Holocene thermokarst dynamics in Central Yakutia – A multi-core and robust grain-size endmember modeling approach

Authors:

Mathias Ulrich[1*], Heidrun Matthes[2], Johannes Schmidt[1], Alexander N. Fedorov[3,4], Lutz Schirrmeister[2], Christine Siegert[2], Birgit Schneider[1], Jens Strauss[2], Christoph Zielhofer[1]

Affiliations:

[1]Leipzig University, Institute for Geography, Leipzig, Germany
[2]Alfred-Wegener Institute Helmholtz Center for Polar and Marine Research, Potsdam, Germany
[3]Melnikov Permafrost Institute, SB RAS, Yakutsk, Russia
[4]North-Eastern Federal University, Yakutsk, Russia
[*]Corresponding author: Mathias Ulrich, Institute for Geography, Leipzig University, Johannisallee 19a, 04103 Leipzig, Germany. Email: Mathias.Ulrich@uni-leipzig.de

Highlights

- Small thermokarst lakes and basins grew rapidly during the Holocene Thermal Maximum
- Short-term phases of forcing climate lead to very active thermokarst processes
- Endmember analysis reveals different depositional environments in growing lakes
- Distal and proximal depositional and post-sedimentary conditions are differentiated
- Sedimentological and biogeochemical characteristics are weakly correlated

Abstract:

Differentiating thermokarst basin sediments with respect to the involved processes and environmental conditions is an important tool to understand permafrost landscape dynamics and scenarios and future trajectories in a warming Arctic and Subarctic. Thermokarst basin deposits have complex sedimentary structures due to the variability of Yedoma source sediments, reworking during the Late Glacial to Holocene climate changes, and different stages of thermokarst history.

Here we reconstruct the dynamic growth of thermokarst lakes and basins and related changes of depositional conditions preserved in sediment sequences using a combination of biogeochemical data and robust grain-size endmember analysis (rEMMA). This multi-proxy approach is used on 10 sediment cores (each 300-400 cm deep) from two key thermokarst sites to distinguish four time slices that describe the Holocene thermokarst (lake) basin evolution in Central Yakutia (CY). Biogeochemical proxies and rEMMA reveal fine-grained sedimentation with rather high lake levels and/or reducing conditions, and coarse-grained sedimentation with rather shallow lake levels and/or oxidizing (i.e. terrestrial) conditions in relation to distal and proximal depositional and post-sedimentary conditions. Statistical analysis suggests that the biogeochemical parameters are almost independent of thermokarst deposit sedimentology. Thus, the biogeochemical parameters are considered as signals of secondary (post-sedimentary) reworking. The rEMMA results are clearly reflecting grain-size variations and depositional conditions. This indicates small-scale varying depositional environments, frequently changing lake levels, and predominantly lateral expansion at the edges of rapidly growing small thermokarst lakes and basins. These small bodies finally coalesced, forming the large thermokarst basins we see today in CY.

Considering previous paleoenvironmental reconstructions in Siberia, we show the initiation of thaw and subsidence during the Late Glacial to Holocene transition between about 11 and 9 cal kyrs BP, intensive and extensive thermokarst activity for the Holocene Thermal Maximum (HTM) at about 7 to 5 cal kyrs BP, severely fluctuating water levels and further lateral basin growth between 3.5 cal kyrs BP and 1.5 cal kyrs BP, and the cessation of thermokarst activity and extensive frost-induced processes (i.e. permafrost aggradation) after about 1.5 cal kyrs BP. However, gradual permafrost warming over recent decades, in addition to human impacts, has led to renewed high rates of subsidence and abrupt, rapid CY thermokarst processes.

Keywords:

Permafrost; Climate change; Holocene Thermal Maximum; Granulometry; Palaeolimnology; Ice complex; XRF; Eastern Siberia; Russia

1 Introduction

Global climate change results in higher temperatures and stronger climate variability in the northern high latitudes and permafrost-affected landscapes (Serreze et al., 2000; Serreze and Barry, 2011; IPCC, 2013; Fedorov et al., 2014a). Positive feedbacks are expected as temperatures warm due to greenhouse gas emissions from rapidly evolving thermokarst lakes and microbial decomposition of permafrost organic material (Walter Anthony et al., 2018), although during the Holocene, thaw lakes also served as carbon sinks (Walter Anthony et al., 2014). Hence, thermokarst lakes and thaw processes in ice-rich permafrost deposits are a crucial part of the global carbon cycle (Grosse et al., 2013; Olefeldt et al., 2016. Strauss et al., 2013, 2017). According to e.g. Stendel and Christensen (2002) the active layer (i.e. the seasonal thaw layer) thickness in the Northern Hemisphere will increase by 30 % to 40 % by the end of the 21st Century. Regions with high ground-ice content, such as the Lena-Aldan interfluve in Central Yakutia (CY) (Soloviev, 1959, 1973), will therefore be particularly affected by high thaw and subsidence rates and the resulting ecosystem change (Fedorov et al., 2014b; Ulrich et al., 2017a). Thermokarst is the strongest permafrost degradation process in areas with high ground-ice content and results in a dissected landscape consisting of differentially aged thermokarst basins and lakes (Czudek and Demek, 1970; Tomirdiaro, 1982).

Thermokarst landscapes cover more than 60 % of the ice-rich permafrost domain (Olefeldt et al., 2016). This coverage makes them a key player in permafrost ecosystems and highlights the importance of understanding these basins as a legacy of permafrost degradation after the Late Glacial Maximum (LGM). Regional thermokarst landscapes have been studied, and formative processes have been hypothesized by Soviet scientists using the example of CY thermokarst landscapes (e.g. Soloviev, 1973; Katasonov et al., 1979; Bosikov, 1998). Nevertheless, a knowledge gap remains and is addressed in this study by using spatially extensive sedimentological analyses to decipher Late Glacial to Holocene small-scale processes as well as related depositional and environmental conditions. The questions of how and when large thermokarst (lake) basins (i.e. alases; dry, grass-covered basins within the Taiga forest) were formed and how they evolved during the Holocene are still the subject of contemporary research (Pestryakova et al., 2012; Nazarova et al., 2013; Ulrich et al., 2017b); it is necessary to answer these questions in order to understand current and to predict future thermokarst processes.

Several studies of Late Glacial to Holocene thermokarst lake sediments have focused on northern and eastern Siberia (Andreev et al., 1997; Katamura et al., 2006, 2009; Popp et al., 2006; Biskaborn et al., 2013a,b, 2016; Schleusner et al., 2015; Klemm et al., 2016; see Fig 1a), Alaska (Farquharson et al., 2016; Lenz et al., 2016; Jongejans et al., 2018) and Canada (Lenz et al., 2013; Fritz et al., 2018). The understanding of thermokarst processes is often linked to their spatial distribution (e.g., Morgenstern et al., 2011) as well as to the sediment archives (e.g., Morgenstern et al., 2013). Elucidating the sedimentary characteristics in combination with the elemental composition and deduced biogeochemical properties (Bouchard et al., 2011, 2017; Biskaborn et al., 2013b) is, moreover, important for understanding geomorphological thermokarst processes. However, a statistical (i.e. manual) evaluation of polymodal grain size distribution (GSD) according to e.g. Folk and Ward (1957) only allows limited interpretation and discussion of sediment origin and transport conditions (Hartmann, 2007). But polymodal GSDs are typical for natural sediments, in general, due to different sediment sources as well as different transport and accumulation processes (e.g., Weltje and Prins, 2007), and typical of postsedimentary treatments and ice-rich permafrost deposits of the Yedoma type, in particular, due to their polygenetic origin (Schirrmeister et al., 2011a; 2013). A statistical analysis based on the eigenvalues of a grain size dataset was therefore recognized as a promising approach (e.g., Flemming, 2007). Endmember (EM) modeling is a widely used method for process-oriented differentiation of multimodal GSDs (e.g., Weltje and Prins, 2003; Hamann et al., 2008; IJmker et al., 2012; Dietze et al., 2014; Nottebaum et al., 2015) but it has very rarely been applied to permafrost and in particular to thermokarst deposits so far (Strauss et al., 2012; Klemm et al., 2016; Schirrmeister et al., 2017; Macumber et al., 2018). EM modeling uses the eigenvalues of a dataset and reduces the dimensions of the data space by applying a factor analysis method (Veganzones and Grana, 2008; Dietze et al., 2012). Finally, recurring patterns in the source record are grouped into specific classes (i.e. EMs). The statistical method of rEMMA thus offers meaningful genetic results to differentiate GSDs for reconstructing sedimentological and paleoenvironmental conditions (Weltje and Prins, 2003, 2007; Dietze et al., 2014; Dietze and Dietze, 2019).

By applying a multi-proxy approach in connection to rEMMA using ten sediment cores from two thermokarst basins with different geocryolithological conditions, we aim to identify and to interpret characteristic patterns in GSD and biogeochemical data of thermokarst deposits in relation to age, location, geomorphology, and main depositional conditions of the different drilling sites. The main objectives of this paper are (i) the lithostratigraphic characterization of different kinds of thermokarst sediments using a multi-proxy approach and rEMMA; (ii) the reconstruction of local geomorphological processes responsible for the individual development of CY thermokarst basins during the Late Glacial and Holocene periods; and (iii) the detection of regional climatic imprints with respect to similarities in thermokarst development, considering previous paleoenvironmental reconstructions in Siberia.

2 Regional setting

CY is bounded by the Lena and Aldan rivers and located in the east-Siberian Subarctic. The region is a special case due to the lack of lowland glaciation during the late Pleistocene, a strong continental climate setting, and continuous permafrost with depths reaching several hundred meters (Fig. 1, Czudek and Demek, 1970). The active layer reaches depths of about 2.0 m in grassland areas but has much lower depths below Taiga forest (e.g. Fedorov et al., 2014b). Taliks (i.e. bodies of unfrozen ground) usually exist only below beds of major rivers and below lakes where the water is deeper than winter lake-ice thickness. Isotherm subsurface temperatures in the region at 10-15 m depth usually range from about -3°C below dense forest cover to about -2°C below grassland areas (Fedorov et al., 2014b). The region is characterized by low annual precipitation of 223±54 mm and a mean annual air temperature (MAAT) of -9.8±1.8 °C (1910 – 2014 average at Yakutsk weather station, NOAA National Climatic Data Center, http://www.ncdc.noaa.gov/, Station ID: GHCND:RSM00024959). With the exception of stable Siberian anticyclones during winter time, the wind and weather conditions in CY are determined by cyclonic weather conditions that run from west to east across the region. During the winter period from September to May wind conditions are relatively calm. Slightly stronger winds occur during the short summer period from June to August (Péwé and Journaux, 1983). A 75-year record at Yakutsk indicates a mean annual wind velocity of 2.4 m/s (Gavrilova, 1973). For our study region, the Global Wind Atlas (2018) indicates an average wind speed of about 4 m/s.

The Lena-Aldan interfluve region is a low-relief landscape. Geomorphological processes are linked to Holocene and current thermokarst phenomena (Brouchkov et al., 2004; Katamura et al., 2006; Fedorov and Konstantinov, 2009; Iijima et al., 2014; Séjourné et al., 2015; Ulrich et al., 2017a, b). Thermokarst basins (i.e. alases) and thaw lakes are widespread, typical landscape features in this region (e.g., Soloviev, 1973; Fig. 1b). Larch forest with inclusion of pine and birch trees typically dominates the CY vegetation. Thermokarst basins form islands of grasslands within the taiga forest that are dominated by steppe-like to swamp communities, depending on edaphic factors within the basins (Mirkin et al., 1985; Desyatkin, 2008).

Major parts of the Lena-Aldan interfluve region are covered by ice-rich fine-grained late Pleistocene sediments containing up to 80 % ice by volume, mainly in the form of huge syngenetic ice wedges. These Yedoma deposits form the forest-covered Yedoma uplands surrounding the thermokarst landscapes. Several terraces above the major rivers are differentiated due to cryolithology and sediment genesis in the Lena-Aldan interfluve region (Soloviev, 1959, 1973; Fig. 1c). Typical well-developed thermokarst basins and lakes in different evolutionary stages are mainly found on the Tyungyulyu and Abalakh terraces. Both terraces are characterized by thick ice-rich deposits (more than 40 m thick in some places) with different cryolithological conditions and characteristics (Soloviev, 1959; Fedorov and Konstantinov, 2003, 2009; Ulrich et al., 2017a).

Two thermokarst basins were chosen as study sites that were considered representative for the respective terraces. Both are located about 80 km southeast from Yakutsk (Fig. 1c). The Khara Bulgunnyakh (KB) alas (Lat: 61,836680, Long: 130,646150; Fig. 2a) is part of a larger alas system and is located about 130 m a.s.l (above sea level) on the Tyungyuluy Terrace. The KB alas is about 1000 to 1500 m in diameter and about 6 to 10 m deeper than surrounding Yedoma uplands. Three large pingos within the KB alas reach heights of 8 to 12 m and diameters of 50 to 100 m. They are surrounded by very shallow lakes. The alas system was investigated by a Russian research group in the 1970s (Katasonov et al., 1979). They suggest that its evolution started around 12-10 thousand years ago because they found stalks of reed grass in the northwest of the alas system below 3.0 m depth that has been dated to a ^{14}C age of 9120±200 yrs BP (10,261 ± 289 cal yrs. BP).

The Yukechi (YU) alas (Lat: 61.764950, Long: 130.465260, Fig. 2b) is located on the Abalakh Terrace at about 202 m a.s.l. The YU alas is about 300 to 500 m in diameter and about 10 to 15 m deep. Two larger lakes and one small shallow pond existed within the alas. The area around the YU alas is characterized by many young thermokarst features and lakes, indicating current intensive thermokarst development. In particular, small, young thermokarst lakes are ubiquitous on the Yedoma uplands. Many of these Yedoma lakes were evidently developed anthropogenically (e.g. in former agricultural areas) (Fedorov et al., 2014b; Ulrich et al., 2017a). The YU alas and its surroundings have been monitored for several decades by the Melnikov Permafrost Institute in Yakutsk (Bosikov, 1998; Fedorov and Konstantinov, 2003, 2008, 2009; Fedorov et al., 2014b), but the exact timing and rate of YU alas evolution during the Holocene remain unclear.

3 Material and methods

3.1 Permafrost coring and sampling

At both study sites five cores were drilled in August 2013 from the dry basin ground (Fig. 2). The drilling and sampling design follows a transect sampling design covering the major alas landscape units (Fig. 3).

Thus, for each study site at least one to three cores were taken from the basin centers (KB3, KB7, and YU2, YU3, YU4) and one or two cores from marginal basin areas (KB1, KB4, and YU1). The KB7 core was taken on the top of a small pingo in the basin center. Several analyses of KB7 core content including ostracods, chironomids, and pollen are already published (Ulrich et al., 2017b). Addionally, at each study site one core was taken from the center of a neighboring smaller drained thermokarst basin that is connected to the main basin (KB6, YU5).

If possible, an active layer pit was dug first and the frozen core was drilled from the permafrost table. This was often necessary due to difficult drilling conditions within the active layer. Sediment samples were then additionally taken from the active layer pit. Hereafter, they are also discussed as part of the sediment cores. Data gaps especially within the active layer are the result of core losses during drilling. All sediment cores were drilled down to 300 - 400 cm below surface (bs). Each core segment (about <20-30 cm long) was cleaned, described, and photographed according to sediment composition, color, and cryolithological properties following French and Shur (2010). Subsequently, the cores were continuously sampled at <10 to 20 cm intervals, the samples were packed in plastic bags, and transported to the laboratories.

3.2 Laboratory sedimentological and biogeochemical analyses

We analyzed sedimentological and biogeochemical parameters for all sediment samples after freeze-drying. For each analytical method, individual subsamples were used. Grain-size analyses were carried out using carbonate-free (treated with 10% HCL) and organic-free (treated with 35% H_2O_2) subsamples using a laser particle analyzer (Beckmann Coulter LS 200) according to DIN ISO 11277. The proportions of sand, silt, and clay fractions are given as sums between 2 mm and 63 µm, <63 µm and 2 µm, and <2 µm, respectively. Grain-size parameters such as the geometric mean of the respective particle size distribution in µm and sorting in φ were determined according to Folk and Ward (1957) with the Gradistat software (Version 8.0, Blott and Pye, 2001). The mass-specific magnetic susceptibility (MS) was analyzed using a Bartington MS2B dual-frequency sensor. The values are expressed in SI units (10^{-6} m^3 kg^{-1}).

Total carbon (TC) and total nitrogen (TN) were measured with a Vario EL cube elemental analyzer and are given as weight percent (wt%). The total inorganic carbon (TIC) content was taken from carbonate measurements, which were conducted using the Scheibler method on an Eijkelkamp Calcimeter apparatus by continuously adding 4 N HCL to a subsample until the CO_2 outgassing reaction ceased. TIC is then calculated by dividing the percent calcium carbonate (CaCO3) with 8.33. The total organic carbon (TOC) content was determined by subtracting TIC from TC. The TOC/TN ratio is expressed as the quotient of TOC and TN weight percentages but is given as mass ratio by dividing them by 1.167 (the ratio of atomic weights of N and C; Meyers and Teranes, 2001). Stable carbon isotopes ($\delta^{13}C$) were measured on carbonate-free subsamples with a Delta V Advantage isotope mass spectrometer (ThermoFisher Scientific™) coupled with a ConFlo IV Interface and a Flash 2000 IRMS Elemental Analyzer. The values are expressed in delta per mil notation (δ ‰) relative to the Vienna Pee Dee Belemnite (VPDB) Standard.

Bulk samples from the recovered cores were analyzed according to Zielhofer et al. (2017) with a Spectro Xepos XRF (X-ray fluorescence) device. For XRF sample preparation bulk subsamples (8 g) were homogenized with a vibratory Retsch mill MM 200. Pressed pellets were prepared using a Vaneox press at 20 t for 2 min. Measurements were conducted in a He atmosphere.

According to Davison (1993), Bouchard et al. (2011), and Biskaborn et al. (2013a) only a few elements can be used for tracking thermokarst processes. We chose the elements Mg, S, Ca, Mn, Fe and their ratios for detailed discussion of sediment properties and depositional conditions and dynamics during thermokarst (lake) processes and basin evolution.

3.3 Radiocarbon dating

Radiocarbon dating was performed on 34 sediment samples from eight cores at the Curt-Engelhorn-Centre of Archaeometry (Mannheim, Germany) using the Accelerator Mass Spectrometer (AMS) technique (Tab. 1). The treatment was conducted with the Acid-Base-Acid method and the samples were measured in the MICADAS accelerator. Hand-picked terrestrial plant remains, wood fragments, and charcoal was dated only from 14 sediment samples. For 20 samples soil organic carbon was dated using bulk sediment samples due to the lack of organic macro remains within samples. Finally, the conventional ^{14}C ages were calibrated using the INTCAL13 data set (Reimer et al., 2013) and SwissCal 1.0 (L. Wacker, ETH Zürich). The ^{14}C ages are normalized to $\delta^{13}C$ = -25‰ (Stuiver and Polach, 1977).

3.4 Grain-size EM modeling and statistical analysis

The GSDs derived for each sample were used in an EM modeling approach to try and unmix the polymodal GSDs into characteristic grain-size subpopulations which can be attributed to sedimentary processes and conditions. EM modeling reduces the dimensions of a data space (the GSDs) using the method of factor analysis, where eigenvalues are used to extract recurring patterns in the initial data set (the EMs) (Veganzones and Grana, 2008). For rEMMA, the open source R-package EMMAgeo following Dietze et al. (2012, 2014, 2016) and Dietze and Dietze (2019) was used, which contains the following steps: (1) Before conducting the actual EM analysis, a grain size data matrix is constructed, containing the grain size distributions (columns) for each sample (rows), which is then rescaled to constant row sums. Then, a weight transformation is applied according to Klovan and Imbrie (1971), using a weight transformation parameter to yield a weight matrix that is not biased by variables with large standard deviations. To allow the extraction of robust EMs, the ranges of the weight transformation parameter and the minimum and maximum number of possible EMs are identified from the measured data set. (2) EM modeling is performed for all combinations of the weight transformation parameter and the number of EMs. Robust EMs (rEMs) are defined as grain-size subpopulations that appear independent of the chosen model parameters and have an overall explained variance >50%. (3) In order to quantify the uncertainties associated with the contribution of each grain size class to each mean rEM, an uncertainty estimate is calculated from the spread of the contributing EM. (4) The scores for each sample, which provide a quantitative estimate of how much a rEM contributes to a sample, are calculated for the mean rEM loadings. An uncertainty estimate for the scores is calculated via a Monte-Carlo simulation. From the rEM loadings and scores, sample and class-wise explained variances are calculated to assess the overall quality of the chosen model.

Finally, a principal component analysis (PCA) was performed on all rEM scores and sample biogeochemical parameters to examine connections and relationships between sedimentology and biogeochemistry of the thermokarst deposits. The PCA was carried out using R (R Core Team, 2014). Because of the very different nature of the scores from the rEMMA and the biogeochemical analyses, all variables were standardized by substracting the mean and scaling to the actual data range of the specific variable. Note that this means that variances are not equal to 1 for all variables. A four-fold cross validation approach was used to assess the number of relevant PCs, using the R package missMDA (Josse and Husson, 2016). The resulting ordination diagram presents standardized metric scores and expresses the relationship among metrics as correlations. Additionally, all core samples are projected onto the ordination graph for interpretation purposes only, because they do not affect calculations; sample scores on the first and second principal component (PC1 and PC2, respectively) were plotted against core depth.

4 Results

4.1 Geochronology

The results of dating 34 samples from eight cores shown in Table 1 indicate a clear difference in age between bulk organic material and terrestrial organic macro remains. Overall, macro remain and bulk radiocarbon dates of YU study site samples are older than dates of KB site samples (Fig. 3). While almost all macro remains show middle to late Holocene ages, with the exception of two samples from cores YU3 and YU5, all bulk samples, except one sample from the YU2 core, were dated between Late Glacial and early Holocene ages (Tab. 1). This age discrepancy is attributed to the different carbon sources of the dated material and will be independently considered in further geochronological discussions. Since there is a very low TIC content in all cores (0.1 to 1.7 wt%, Appendix A), carbonate-derived reservoir effects are suggested to be insignificant.

For the KB study site, macro remain ages from the central basin have been derived only for the KB7 core. The five KB7 macro remain samples taken between 320 and 60 cm bs show middle Holocene radiocarbon dates between 6582±78 and 5752±102 cal. yrs. BP (see also Ulrich et al., 2017b). For the KB1 core at the basin edge, three late Holocene macro remain ages range between 3314±62 and 1812.5±72.5 cal. yrs. BP (between 243 and 125 cm bs, respectively). One sample (92 cm bs) of the KB6 core located centrally within the small drained basin orginated from an organic inclusion with wooden remains and was dated to 3316±61 cal. yrs. BP. The late Pleistocene and Late Glacial to early Holocene bulk ages for the KB study site generally decrease from the basin center (KB3, KB7) to the basin edge (KB1) (Tab. 1). The KB3 core show the highest ages at the KB study site and continuously upward decreasing bulk ages between 38,355±615 and 12,902.5±184.5 cal yrs BP.

For all YU study sites, five radiocarbon dates were derived from macro remain samples. Two samples from the basin's center (YU3) show ages of 34,865±235 cal. yrs. BP at 185-170 cm bs and 3975±102 cal. yrs. BP at 40-36 cm bs. One macro remain sample from the YU1 core (110-105 cm bs) at the basin edge was dated to 4606±175 cal yrs. BP. Another two samples from the YU5 core of the small drained neighboring basin (Figs. 2b and 3) show strong differences: While the macro remain sample from 222-210 cm bs was dated to the late Pleistocene time period (39,340±650 cal. yrs. BP) and thus represents the oldest macro remain sample from both study sites, another sample from 40-20 cm bs shows a modern age but may have been contaminated during drilling, which is even more probable considering the bulk sample age from same depth (see Tab. 1). The YU bulk ages show a rather unclear division between the central and the marginal parts of the basin (Tab. 1). Late Pleistocene to middle Holocene bulk ages are shown by the basin center cores YU3 and YU2, while the dates from the lower part of the YU1 core at the basin edge show a strong inversion of downward decreasing Late Glacial ages. This probably indicates the strong redeposition of Yedoma deposits during the lateral expansion of the thermokarst basins (see discussion below). The YU5 core from the neighboring small basins, however, shows continuously upward decreasing late Pleistocene bulk ages between 41,625±405 and 27,625±165 cal yrs BP.

4.2 Cryolithology, Sedimentology, and Biogeochemistry

As a result of our laboratory analysis of sedimentological and biogeochemical parameters, we indentify different facies within the thermokarst deposits from the basin edges and from the central basin parts, which will be described separately for each study site. Generally, all KB and YU sediment sequences were composed of visibly homogeneous silt-dominated deposits with varying but generally low amounts of organic inclusions and varying ice contents (Fig. 4). Usually, the upper half of all sediment cores was characterized by rust-stained brownish-greyish deposits. These horizons generally continued downwards in the frozen core material with some blackish streaky layers and spots (Fig. 4a-f). The lower frozen parts of the cores were usually dominated by dark grey to dark olive-green sediments, interrupted by blackish spots and streaky layers (Fig. 4g-l), which were less pronounced within the YU cores. Furthermore, sediment layers in the basin edge cores (KB1 and YU1) showed bent or mixed layers in relation to topography changes on the thermoterraces (Fig. 3).

The ground-ice content often increased with depth and was represented by parallel to non-parallel lenticular-layered to reticulate cryostructures, which reached a thickness of up to 6 mm in some deeper core parts (Fig. 4). Exceptions here were represented by the cores from the neighboring small basins (KB6 and YU5). They showed significantly lower ice content and fewer to no cryostructures in their frozen parts. In addition, all cores from the YU basin center (YU2, YU3, YU4) were unfrozen. This is due to an existing talik below the YU alas. Post-cryogenic structures in the lower core parts show once-frozen, ice-rich sediments. In particular, the YU2 core is currently strongly influenced by ground water changes due to the nearby lake and showed pronounced redox properties in the sediment (Fig. 4a).

4.2.1 Sedimentological and biogeochemical results of the KB thermokarst basin

The KB thermokarst deposits are composed of uni-, bi-, tri-, and polymodally distributed, poorly to very-poorly sorted, very-fine to fine sandy medium-to-coarse silt. The grain-size characteristics differ between the horizons of a core as well as between the drilling sites (Fig. 5). The GSDs and MS values of the KB3 core from the basin center show little variability (Fig. 6). The KB3 GSDs are bimodal with main peaks in the coarse silt fraction. The second mode can be found in the coarse clay to very-fine silt. The grain-size mean for the KB3 core is 16.7±1.1 µm (see Appendix A, Table S3). GSD peaks of the KB7 core from the small pingo top are located mainly in the coarse-silt fraction, but all samples show high variability (mean 25.2±6.8 µm; Tab. S4). Additional minor but distinct peaks in the fine-sand fraction are mainly found in samples from the upper and lower KB7 profile, while minor peaks in the coarse clay to very-fine silt fraction are predominantly found in the middle of the core. The MS decreases upwards (0.3 to 1.3 x 10^{-6} m^3 kg^{-1}) with a distinct peak of 2.2 x 10^{-6} m^3 kg^{-1} at 285–258 cm bs. The GSDs of the KB1 and KB4 basin edge cores show main peaks in the coarse silt fraction with generally two minor peaks in the fine sand and clay fractions (Fig. 5). The grain-size means for KB1 and KB4 are 23.5±5.8 µm and 18.0±2.0 µm, respectively (Tabs. S1 and S2). Increased amounts of sand in the upper and lower KB1 profile and in the upper KB4 profile correspond to increased MS values. The GSDs of the KB6 core from the neighboring smaller basin also show high variability with a grain-size mean of 23.3±8.7 µm (Tab. S5) and main peaks in the coarse silt fractions. MS values show comparably less variability, slighty decreasing upwards (1.2 to 0.6 x 10^{-6} m^3 kg^{-1}).

The KB biogeochemical records and elemental composition show some pronounced differences in relation to the sedimentation history and geomorphological location of the individual sediment profiles. With the exception of the KB7 core, the TOC values of all cores are comparably low with hardly any variations. In contrast, the upper half of the KB7 core shows upwardly increasing TOC values that reach a high value of 10.1 % at the active layer bottom (Fig. 6; mean 3.6±2.9 %). The variations of TOC/TN ratios are higher for the KB basin edges (KB1: 7.9 – 14.0, KB4: 6.6 – 15.1) than for the basin centers (KB3: 6.3 – 11.2, KB7: 7.1 – 10.5) and the KB6 core in the small neighboring basin (5.8 – 8.6). The $\delta^{13}C$ values are, however, homogeneous for KB3 (-25.4 to -24.4 ‰) and KB1 (-25.1 to -24.1 ‰) and show little variation in KB4 (-26.2 to -24.1 ‰), but the values are lower and upwardly decreasing in KB7 (-28.8 to -25.4 ‰) and KB6 (-27.2 to -24.5 ‰). The $CaCO_3$ content is strongly negatively correlated with the Ca/Mg ratio in all KB core profiles, indicating that Ca is largely bound as $CaCO_3$. $CaCO_3$ concentration shows relatively strong variations and several pronounced peaks were found in all cores which ranged between 0.0 and 7.4 % with highest values reached in the lowest parts of KB7 and KB3 (basin center) and the middel core parts of KB4 (basin edge). Strong differences between the coring locations and within the cores can be seen in the S contents of the KB cores (Fig. 6). Usually, peaks in S contents coincide with the above-described black layers and spots in the middle and lower parts of the KB sediment cores. With the exception of KB7, the Fe/S ratio is low in the frozen core parts but increases strongly in the active layer of all KB cores. The KB7 core, however, shows a very narrow Fe/S ratio, but the ratio is higher at the profile bottom and decreases upwards with two small peaks at 258-143 cm bs and at 70-30 cm bs. The Fe/Mn ratio shows strong variation in the KB1 and KB4 basin edge cores and the KB3 basin center core. Variations are smaller in KB6 and the ratio increases stepwise in KB7.

4.2.2 Sedimentological and biogeochemical results from the YU basin

The GSDs of YU thermokarst basin deposits are differentiated within and between the cores, similar to the KB results (Fig. 5). The GSDs of the YU2 core from the lowest part of the basin center show variations with bimodal distributions, main peaks in the coarse silt fraction, and secondary modes in the coarse clay to very-fine silt. The grain-size mean is the lowest of all cores at 15.4±1.5 µm (Tab. S7). The grain-size mean and GSD variability is a little higher for the other basin center cores YU3 and YU4; 17.3±3.5 µm and 19.8±3.9 µm, respectively (Tabs. S8 and S9). Both cores, moreover, show main peaks in the coarse silt fraction, with generally minor peaks in the fine sand and clay fractions. However, the YU3 GSD variability is determined by a few sandy samples and mostly stronger secondary modes in the coarse clay fraction, while the YU4 GSDs are characterized by more distinct secondary modes in the fine sand fraction. Besides a strong decrease in the upper part of core YU2, the MS shows little variation in the basin center sediments. The GSDs of the YU1 core from the thermoterrace at the basin edge show high variability from uni- to polymodal distributions with main peaks in the coarse silt fraction and fluctuating secondary peaks in the fine sand and coarse clay to fine silt fractions (Fig. 5). The grain-size mean is 21.1±5.9 µm (Tab. S6). Similar to the KB basin edges, increased amounts of sand in the upper and lower part of YU1 correspond to increasing MS values. Compared to the KB6 core, the YU5 core from the neighboring small drained basin shows little GSD variabilty. The lower half of the YU5 core is characterized by higher amounts of fine sand while the upper half shows higher clay contents. The grain-size mean is 19.0±3.0 µm (Tab. S10).

The biogeochemistry of the YU sediments shows some differences from the KB thermokarst basin deposits (Fig. 7). The TOC content in the YU basin is higher on average than in KB. TOC increases upwards from 0.5 % to 4.0 % in the uppermost part within the basin edge core YU1. In the basin center, YU3 shows lower downward increasing values between 0.3 and 1.3 %. The TOC content peaks in the uppermost part of YU2 to 2.3 % and increases slightly downwards in the YU4 core, ranging between 0.3 and 2.6 %. The YU5 core TOC content is more stable, ranging between 1.3 and 2.5 %. The variations of the TOC/TN ratio are generally less at the YU study site than at the KB study site. But similar to KB, variations are larger at the basin edge (YU1: 5.6 – 11.2) than in the center area of the YU basin (YU2: 7.2 – 9.6; YU3: 6.2 – 8.3; YU4: 6.0 – 8.5). The ratio, however, increases slightly upwards in the YU5 profile (6.6 – 10.0). The $\delta^{13}C$ values are homogeneous in all cores, averaging around -25 ‰. Only the uppermost part of core YU2 shows a strong decrease of $\delta^{13}C$ to -29.2 ‰. Similar to KB, the $CaCO_3$ content in the YU cores is negatively correlated to the Mg/Ca ratio. However, the $CaCO_3$ content is higher on average in YU cores than in KB cores, ranging between 0.8 and 13.8 % (Fig. 7). With the exception of the YU5 core, the S contents are on average lower in the YU than in the KB sediment sequences and differences between basin center and edge are smaller, but some variations within the YU cores are obvious as well. The higher average TOC content at the YU site and the generally stronger correlation of the S contents with TOC as well as the visible absence of significant black streaks in YU sediments suggest that there is a larger amount of organically bound S within the YU sediment sequences. The Fe/S ratio shows a different behavior within the YU sediment sequences than within the KB cores. Within the basin center, the Fe/S ratio is narrower and shows less variation in the YU3 core but shows an upwards increase and higher ratios in the YU2 and YU4 cores with a strong peak at about 80 to 100 cm bs; the Fe/S decreases again towards the surface. For YU1 at the basin edge, the Fe/S ratio shows a little more variation with wider ratios in the upper middle core part. The Fe/S ratio is small within the YU5 core and shows less variation. The Fe/Mn ratio in the YU sediment sequences shows less variation than in the KB sequences, but variations are generally largest in YU1 at the basin edge and smallest in core YU5.

4.3 rEMMA

The four final rEMs account for 79.5% of the total variance of all initial variables (i.e. all input GSDs) with modes in various grain-size fractions between clay and medium sand. The unmixed rEMs are characterized by their loadings (Fig. 8). The rEM1 shows its strongest peak in the coarse clay to very-fine silt fraction (mode = 2.9 µm, explained variance (EV) = 24%). rEM1 exhibits some unmixed residuals in the coarse silt and fine sand fraction. rEM2 has a bimodal distribution with residual mode in the fine sand fraction. The main mode is located in the medium to coarse silt fraction at 27.4 µm (EV = 18%), but its slightly left-skewed distribution shows some tendency to increased finer grain sizes. rEM3 shows a distinct unimodal distribution with a high peaked mode in the coarse silt fraction at 39.8 µm (EV = 25%) but it shows some tendency to the coarser grain sizes by a slightly right-skewed distribution. The mode of rEM4 peaks in the fine to medium sand fraction at 176.8 µm (EV = 32%) with some tendency towards the finer grain sizes. The class-wise explained variance in Fig. 8 shows that in particular the very-fine to fine-grained fractions show highest variances.

Calculated mean scores are shown in Fig. 8 with their confidence intervals and in Fig. 9 against depth for each core individually. The scores represent the relative rEM contribution to each sample, i.e. how each sample is composed of a specific rEM. Equal compositions of mostly rEM1, rEM2, and rEM3 with comparatively larger shares of rEM1 and rEM2 over the entire sediment sequences are reflected in particular for the basin centers (i.e. KB3, YU2, YU3). An exception is shown by the KB7 scores, which exhibit strong variations of all rEMs but generally a division of the sediment sequence. While rEM3 and rEM4 dominate the lower half of the KB7 core, the shares of rEM1 and rEM2 are significantly higher in the upper half. The basin edge sediment sequences (i.e. KB1, KB4, YU1) show varying compositions including all rEMs. Smaller contribution of rEM1 in KB1 and YU1 emphasize the proximal accumulation conditions of these sites and the increased influence of coarser basin slope sediments. The higher contribution of rEM1 in the KB4 basin edge core are a sign of comparatively lower erosion at the northern edge of the KB basin than at the eastern edge captured by the KB1 core (Figs. 2 and 3). In contrast, the larger shares of rEM3 and rEM4 in the middle part of the YU4 basin center core (Fig. 9) are probably related to YU4's location at the edge of a flat hill within the YU bottom. The KB6 and YU5 rEM scores show the individual rEM compositions within the neighboring small drained basins. KB6 shows a bulge increase and subsequent decrease of rEM1 und rEM2 in the lower half of the sequence. The upper half shows stronger variations of all rEMs. YU5, on the other hand, is dominated by a homogeneous share of rEM1, rEM2, and rEM3, but also shows higher amounts of rEM4 in three samples from the lower part of the core.

4.4 PCA

The PCA shows two major principal components (PC1 and PC2) that explain 27.9% and 22.3%, respectively, of the total variance of all rEMs and biogeochemical parameters from the KB and YU thermokarst deposit core samples (Fig. 10). PC1 is positively correlated with rEM1, rEM2, and Fe/Mn and negatively correlated with rEM3, rEM4, and MS. PC2 is clearly controlled only by the biogeochemical parameters; it shows positive correlations with S, TOC, Mg/Ca, and TOC/TN, and negative correlations with $\delta^{13}C$, Fe/S, and $CaCO_3$. The core samples projected into the ordination graph show only rough separations. The basin edge core samples (KB1, KB4, YU1) are scattered throughout the complete PC1 axis but are more common on the negative part of the PC2 axis, while the basin center core samples (KB3, YU3) occur more frequently on the positive part of PC1 but more evenly throughout the complete PC2 axis. The YU2 core samples are clustered in the lower right of the ordination plot and the KB7 core samples are broadly scattered on the positive part of the PC2 axis and across the complete PC1 axis. The core samples from the neighboring small basins, KB6 and YU5, as well as the YU4 core sample are scattered across both PC axes.

While PC3-PC5 are considered relevant due to the results of the four-fold cross validation approach, a reasonable physical interpretation is not possible. Ordination plots for all PCs are included in the supplement material (Appendix B, Figs. S1, S2, and S3).

5 Discussion

5.1 Sedimentary properties and biogeochemical characteristics of CY thermokarst deposits

The GSDs and the resulting sorting provide information on the erosion and transport processes as well as on the accumulation conditions of the thermokarst sediments. Assuming that individual transport processes would have led to better fractionation of the grain sizes (e.g., Folk and Ward, 1957), the poor to very poor sorting of all GSDs indicates short transport paths (see Appendix A) or a mixture/overlay of different formation processes (Blott and Pye, 2001).

The subsequent reconstruction of erosion, transport, and sedimentation conditions is thus difficult to perform (Dietze et al., 2012, 2014; IJmker et al., 2012). In the study region, the GSDs of the source sediments from Yedoma deposits are heterogeneous due to their polygenetic formation, leading to polymodal GSDs (Schirrmeister et al., 2011a, 2017; Strauss et al., 2017). The spatial understanding of the local Yedoma structure is thus of great importance for interpreting GSDs in thermokarst deposits (see section 5.2).

In general, coarser grain sizes (especially the fine sand fraction) within the thermokarst (lake) basins point to shorter transport paths after erosion processes along lake shores. Coarser-grained sediments can also be accumulated via longer high-energy transport or by subsidence and in situ accumulation close to the lake center within small thermokarst lake basins. Finer grain sizes like coarse clay are thought to be indicative of distal (to the lake center) transport in larger lakes (e.g. Biskaborn et al., 2013b).

Generally, the MS parameter depends on source rock and/or sediment (Schirrmeister et al., 2011b). We found stronger MS signal variations especially in the basin edge sediments from both study sites (KB1, KB4, YU1) and the lower part of the KB7 core.The reworking of Yedoma deposits under lacustrine conditions may have altered the MS signal in the basin centers, since the magnetizable minerals degrade under reducing conditions, resulting in lower values (Evans et al., 1997; Hanesch and Scholger, 2005). The MS signal therefore also indicates an increase in lacustrine finer-grained detritus (lower MS) or increased terrestrial coarser-grained input (higher MS) (Matasova et al., 2001). In accordance with Schirrmeister et al. (2011c), we also observe that the MS is inversely proportional to the sediment TOC.

The TOC proportion is a main parameter in the analysis of thermokarst sediment developmental history (e.g., Walter et al., 2007; Lenz et al., 2016; Bouchard et al., 2017). Assuming constant input, high TOC values in ice-rich permafrost deposits generally reflect low organic matter degradation during the past and high quality in the sense of future microbial degradation (Strauss et al. 2015). This is generally typical for polar regions, as microbial decomposition of organic matter has limited amount of time before freezing, thus it generally ceases at low temperatures and organic matter is preserved for a long time in the frozen state (Strauss et al., 2013, 2017). Generally, we measured comparably low TOC values in the KB and YU alas thermokarst deposits, suggesting low organic carbon input or strong post-sedimentary organic carbon decomposition, at least within the drilled 300 – 400 cm bs. Based on the fact that there is no depth-dependent trend in some cores, we assume a relatively low organic carbon input compared to other thermokarst and Yedoma landscapes (Strauss et al., 2013). The exceptionally high TOC values in the upper half of the KB7 profile are suggested to be related to high bioproductivity and a nutrient oversupply within a very fast-growing thermokarst lake during the mid-Holocene at this specific site (Ulrich et al., 2017b).

Organic carbon transport pathways (e.g. lacustrine or terrestrial) into the formerly existing thermokarst lake can be identified by combined analysis of $\delta^{13}C$, the TOC/TN ratio, and TOC (e.g. Meyers and Teranes, 2001). High TOC/TN ratios around 20 are produced by cellulosic, low-protein, vascular land plants. In contrast, narrow TOC/TN ratios between 4 and 10 are produced by phytoplankton or algae (Meyers, 1994; Meyers and Lallier-Vergès, 1999). Ratios between these very high and very low values as shown in our data can be seen as a mixture of different entry paths. However, especially in oligotrophic lakes, the TOC/TN ratio can be reduced by organic matter decomposition under oxic conditions, because carbon is preferred over nitrogen (Meyers and Lallier-Vergès, 1999; Meyers and Teranes, 2001). For the thermokarst deposits studied here, higher TOC/TN values have been interpreted as greater terrestrial input, whereas lower values have been considered as greater lacustrine input and/or post-sedimentary carbon decomposition (Meyers, 1994; Biskaborn et al., 2013b; Lenz et al., 2013).

The $\delta^{13}C$ values provide information about plant metabolism because sedimentary organic matter $\delta^{13}C$ values are generally very similar to those of the parent vegetation and post-sedimentation of carbon isotopes is therefore negligible (O'Leary, 1981; Melillo et al., 1989). Thus, we interpreted very low values as an indication of increased bioproductivity. This is obvious in the upper part of the KB7 and YU2 profiles. Finally, different sedimentation milieus can be derived from the TOC/TN– $\delta^{13}C$ relationship (Fig.11), which reflects organic matter origin (e.g., Meyers and Teranes, 2001). This relationship shows a shift from lacustrine algae to terrestrial plants in several samples from the KB1 and KB4 basin edge cores as well as within the lower and upper part of the YU1 core and with decreasing profile depth in the YU5 core. Otherwise the TOC/TN– $\delta^{13}C$ relationship suggests mainly lacustrine sediment origin for great parts of the KB and YU drilling locations (Fig. 11).

S together with phosphorus (P) contents can be used as a proxy for organic entry in thermokarst (lake) deposits (Bouchard et al., 2011). The P content, however, shows only weak correlations with the TOC in our drilled sediments and little variations (see Appendix A). The S content show more connections to TOC but higher S contents also often corresponds with black streaks and spots, especially in the KB sediment sequences. These streaks are interpreted as iron sulfide (FeS) precipitation by iron hydroxide reduction. This is bacterially mediated under anoxic conditions in relatively shallow warm waters and can therefore be seen as evidence of reducing conditions (Siegert, 1979, 1987; Biskaborn et al., 2012). Since the streaks and spots do not follow stratigraphic boundaries, the precipitation of this compound is considered to be post-sedimentary.

$CaCO_3$ can reach the lacustrine sediment archive via several paths. Generally, biogenic and geogenic carbonate origin can be differentiated. The biogenic part is usually formed by aquatic invertebrates like molluscs or ostracods in thermokarst lakes (e.g., Wetterich et al., 2005, 2008). Geogenic formation in CY thermokarst deposits is probably the result of authigenic origin in Yedoma deposits, which are usually rich in carbonate (Katasonov et al., 1979; Schirrmeister et al., 2011a). Furthermore; the original mineral supply to growing thermokarst lakes in ice-rich areas such as the Lena Aldan interfluve may be greater than in areas with lower ice contents (Pestryakova et al., 2012). The Mg/Ca ratio in connection with $CaCO_3$ (geo- and biogenic) provides estimations not only about lake level changes (Haberzettl et al., 2007) but also lake temperature, salinity, and photosynthetic activity during summer months. Generally, higher Mg/Ca ratios and lower $CaCO_3$ values in the studied thermokarst deposits were interpreted to reflect higher lake level and vice versa. For instance, CO_2 is often withdrawn from lake water during summertime due to increased water temperatures and photosynthesis, thus shifting the CO_2 equilibrium at pH values around 8 (typical for current thermokarst lakes in the Lena Aldan interfluve region; Pestryakova et al., 2012) towards insoluble $CaCO_3$, increasing the Mg/Ca ratio (e.g., Ji et al., 2005; Liu et al, 2008). Opitz et al. (2013) discussed high carbonate content in lacustrine sediments of a thermokarst system on the Tibetan Plateau as an indicator of shallow lake levels with corresponding ostracod associations. However, high sediment carbonate content despite the absence of ostracods suggest also decreasing lake levels and increasing salinity due to high evaporation (Liu et al., 2008; Wetterich et al., 2008; Ulrich et al., 2017b).

The Fe/Mn ratio is generally used to evaluate redox conditions in thermokarst lakes (Bouchard et al., 2011, 2014; Biskaborn et al., 2013b). Since Mn is mobilized faster than Fe under anoxic conditions, Fe accumulates residually under reducing conditions (e.g. Davison, 1993). During sedimentation, this ratio is stored and thus preserved as an indicator of the redox milieu during sediment deposition into the lacustrine archive. Increasing Fe/Mn values are thus interpreted as indicative of a change to reducing limnic conditions during sediment accumulation. According to Bouchard et al. (2011, 2014) those anoxic hypolimnic conditions are typical in thermokarst lakes. In contrast, narrow Fe/Mn ratios indicate oxidizing conditions. According to Biskaborn et al. (2013b), these are usually present in shallow waters or better-oxygenated marginal areas of thermokarst lakes. Strong variations in the Fe/Mn ratio as seen in particular in the KB sediment sequences thus suggest continuously changing redox conditions during sedimentation at this location, which indicates either a change in lake level or a change between lacustrine and terrestrial depositional conditions.

The Fe/S ratio was additionally used for qualitative estimations of thermokarst (lake) basin sediment oxygenation. Lenz et al. (2016) discuss increasing Fe/S ratios in relation to increasing lake water oxygenation as being due to increasing water depth and lake size for a thermokarst lake in northern Alaska. They also suggest a relationship between lake-ice cover during wintertime and decreasing Fe/S ratio; reduced water volume over lake sediments favors anoxic conditions, in particular in the near-shore lake zone. The Fe/S ratio is also higher in relation to terrestrial sediment deposition (Lenz et al., 2016), but in light of the data presented here it also seems to increase after lake drainage or water loss and active layer oxygenation.

5.2 Grain-size EM modeling analysis of thermokarst deposits

Overall, the thermokarst deposits at both study sites have been transported and deposited in situ with the Yedoma deposits as source sediment. In particular, the dating of the bulk organic material suggests that there was no remarkable additional sediment input from other sources than the Yedoma deposits during thermokarst evolution at the study sites. For instance, greater Holocene dust entry into the CY thermokarst (lake) basins has not been proven so far. There is still a knowledge gap concerning past wind pattern in the CY region. This is likely connected to the fact that modern wind conditions are relatively calm throughout the year due to the highly continental climate (see section 2). Similar conditions probably existed in East Siberia throughout the Pleistocene/Holocene (Zimov et al., 1995). However, the polygenetic provenance of the Yedoma source sediments is suggested to be partly influenced by aeolian transport beside mainly proluvial, alluvial, fluvial transport, and lacustrine deposition (Soloviev, 1959; Katasonov and Ivanov, 1973; Schirrmeister et al., 2013). Péwé and Journaux (1983) even discuss a dominant eolian component of silty Yedoma deposits in CY.

However, the depositional activities during thermokarst (lake) development overprinted the original depositional processes of the Yedoma source sediments. The final rEMs are therefore the result of the grain size fractionation during thermokarst development. With the rEMMA we were able to detect and to discuss them as single-endmembers, which is hardly possible from the classical measures of grain size properties (Dietze and Dietze, 2019). The rEMMA presented here has yielded four final rEMs (Fig. 8). In general, the final rEMs can be assigned to specific processes, allowing specific sediment transport and accumulation pathways during thermokarst development to be identified (Table 2). The mean scores of the studied core samples (Fig. 9) show the internal variability and thus the sediment history of each sediment sequence taken from different geomorphological sites within the thermokarst basins. Generally, the scores show that the internal variability of basin centers is rather low compared to that of basin edges and the small neighboring basins.

5.2.1 Distal transport dynamics

The rEM1 shows a very coarse-grained clay to very-fine silt. Thus, rEM1 is assigned to a (long) distal transport or a low-energy sedimentation milieu under generally lacustrine conditions (Table 2). In particular, the pronounced rEM1 and the high class-wise explained variance in the range of the very fine particle sizes (Fig. 8) seem to be characteristic for CY thermokarst deposits, and can therefore be used as a distinctive mark to distinguish these from Siberian Yedoma deposits that show less pronounced or absent EMs in the clay fraction of comparable EM analyses (Strauss et al., 2012; Schirrmeister et al., 2017). The rEM2 and rEM3 show silty GSDs. These are background sedimentation signals, since the initial polymodal GSDs of Yedoma deposits are mainly characterized by silty grain sizes (Soloviev, 1959; Schirrmeister et al., 2011a). By comparison, rEM2 tend to have finer grain sizes, whereas rEM3 tend to have coarser grain sizes. Based on the proportion of rEM2 and rEM3 in an individual thermokarst sediment sequence (Fig. 9), it is possible to deduce the sedimentation milieu; rEM2 indicates more distal transport or lower-energy conditions, whereas rEM3 indicates more proximal transport or higher-energy conditions.

5.2.2 Local transport and in situ accumulation processes

At both study sites, rEM4 shows a strong influence of fine sand, which is also contained in the CY Yedoma deposits (Strauss et al., 2012; Schirrmeister et al., 2017). Thus, rEM4 (together with rEM3) is interpreted as an indicator of very short transport pathways and/or in situ accumulation of source sediments during thermokarst initiation. The former occurs especially in the immediate vicinity of eroding lake shores (Table 2).

5.2.3 Indications for thermokarst dynamics

During lake bank erosion, coarser components accumulate at the shores, while the finer grain sizes can be transported to the lake basin center, resulting in grain size fractionation (Biskaborn et al., 2013b). This requires a corresponding lake size, which can be assumed from the rEM score of the KB3, YU2, and YU3 cores (Figs. 2 and 9). With the exception of these core locations, the variations in rEM scores within all sediment cores show alternating homogeneous and heterogeneous fractionation phases, suggesting that a clear sedimentological relationship between a former lake center and corresponding lake shore areas of a single growing thermokarst lake in each basin are difficult to detect at both study sites. This suggests that sedimentary characteristics represent depositional environments of many smaller thermokarst lake basins, which are characterized by changing water levels, poorer sediment fractionation, and changing erosion and thermokarst activities. This is seen in rEM scores from the small neighboring basins (KB6 and YU5) and the small pingo (KB7), in which lacustrine phases that are associated with the dominance of fine-grained sediment accumulation (rEM1 and rEM2) alternate with accumulation phases of coarser sediment (rEM3 and rEM4), probably originating by lateral lake basin expansion and erosive shore processes (Biskaborn et al., 2013b; Lenz et al., 2013). The core locations in the first case became more distal to the sediment source, indicating open water zone enlargement; in the second case the disappearance of the thermokarst lakes and a change to terrestrial depositional conditions is suggested, as seen in the uppermost parts of cores KB6 and KB7. Furthermore, the dominance of coarser rEMs as seen in the scores of the lower parts of these cores is interpreted to represent thermokarst initiation stages, characterized by in situ thaw and subsequent Yedoma deposit subsidence (for e.g. KB7 see also Ulrich et al., 2017b).

5.3 Relationships between sedimentology and biogeochemistry in PCA

The PCA ordination results show that the sedimentological characteristics of the rEMMA results are not or only very weakly correlated to the biogeochemical characteristics of the thermokarst deposits (Fig. 10). Statistical analysis suggests that biogeochemical parameters, with the exception of MS and the Fe/Mn ratio, are independent of thermokarst deposit cryolithology and sedimentology. PC1 is dominated by all rEMs, the MS, and the Fe/Mn ratio, and can thus be considered to largely reflect grain-size variations and depositional conditions. However, while the MS increases with the input of coarser-grained terrestrial source sediments (rEM3 and rEM4), a higher Fe/Mn ratio and thus reducing lacustrine depositional conditions are related to the sedimentation of finer-grained sediments (rEM1 and rEM2) or less detritic input. PC2 is dominated by the biogeochemical parameters with a general separation of organic-indicating and inorganic-indicating parameters. PC2 can thus be considered to indicate post-sedimentary biogeochemical conditions, lake level changes, and organic input.

After plotting the sample scores of PC1 and PC2 against each core depth (Figs. 6 and 7), we can distinguish between fine-grained sedimentation along with rather high lake levels and/or reducing conditions (higher PC1 and PC2 scores), and coarse-grained sedimentation with rather shallow lake levels and/or oxidizing (i.e. terrestrial) conditions (lower PC1 and PC2 scores). An exception is shown by the YU2 basin center core with always negative PC2 scores that are likely the result of an exceptionally high Fe/S ratio due to oxidizing conditions in the active layer and unfrozen talik sediments after lake disappearance (Lenz et al., 2016).

5.4 Late Glacial to late Holocene environmental conditions and thermokarst basin evolution

The sedimentary and biogeochemical composition of thermokarst deposits are complex, but are specifically marked by the alternation of terrestrial and lacustrine phases (Bouchard et al., 2017). The paleoecological and paleolimnological conditions during thermokarst (lake) basin formation are ideally reconstructed by the use of bioindicators such as chironomides (e.g., Nazarova et al., 2013), diatoms (e.g., Pestryakova et al., 2012; Biskaborn et al., 2013a; Bouchard et al., 2013), ostracodes (Wetterich et al., 2008; Ulrich et al., 2017b), pollen (e.g., Katamura et al., 2006; Klemm et al., 2016), cladocera (Frolova et al., 2014, 2017), amoebae (Lenz et al., 2016), and macro remain analyses (Schleusner et al., 2015). Therefore the differentiation of sedimentary facies and palaeoenvironmental changes are usually based on a multi-proxy approach and an adequate geochronology (Bouchard et al., 2017).

Deriving clear age-depth relationships for all the thermokarst sediment sequences from the KB and YU study sites is challenging. Generally, care should be taken with the interpretation of dating of thermokarst deposits due to repeated mixing of brought in Yedoma sediments as well as changing bio-ecological conditions and the rearrangement of already deposited material during thermokarst development (e.g., Biskaborn et al., 2013b; Lenz et al., 2016; Jongejans et al., 2018). Having this in mind and due to the small-scale varying depositional environments discussed above, our core locations cannot be compared by the sediment ages and it is not possible to pinpoint a uniform stratigraphy over the studied sediment sequences (see also Fig. 3, 6 and 7). However, in particular the individual combination of macro remain and bulk ages as well as our multi-core and -proxy approach led us to discuss the Late Glacial to Holocene evolution of thermokarst basins and geomorphological conditions in relation to literature-derived environmental and climatic changes in CY during four time slices (Fig. 12). Following Gaglioti et al. (2014) we assume that our macro remain ages (Tab.1) represent the true sedimentation age of the sediment layer. This make sense because the sampled organic macro remains originate from terrestrial plants (grasses, trees, etc.) that grew in the immediate vicinity of an evolving thermokarst lake and were probably incorporated into thermokarst deposits immediately after they died. Our bulk ages are interpreted as inherited ages of organic matter from the Yedoma deposits, which subsequently subsided or were erosionally redeposited due to thermokarst processes and lake growth (Biskaborn et al., 2013b; Gaglioti et al., 2014).

5.4.1 Late Glacial - Early Holocene thermokarst initiation

It is generally assumed that thermokarst development in CY was initiated by the onset of the Holocene (e.g., Katamura et al., 2006). According to Fradkina et al. (2005), thermokarst lakes began to form near the end of the Late Glacial in the Allerød after about 13,300 cal. yrs. BP. Katamura et al. (2009) suggest thermokarst initiation between 11,000 and 9000 cal. yrs. BP, basing their assumption on increased charcoal and specific pollen findings in thermokarst deposits. Biskaborn et al. (2012) discuss enhanced thermokarst processes in relation to a transition to the mid-Holocene warm period after about 9100 cal. yrs. BP. Following former research results in CY, lake sediment dating by Katasonov et al. (1979) for the KB study site (Fig. 12a; see also above section 2), and in connection with the thermokarst sediment rearrangement that is dated before the mid-Holocene Thermal Maximum (HTM) (see below and Tab. 1), we assume that the onset of permafrost degradation at both study sites also took place at the transition from Late Glacial to Early Holocene. Taking into account the geomorphology of both studied basins, we assume, however, that the KB alas began to develop earlier than the YU alas. Due to the climatic conditions during the Younger Dryas this likely did not happen with the same intensity as later during the middle Holocene.

The late Pleistocene/Holocene transition in CY (ca. 11,.500 – 11,200 cal. yrs. BP) is characterized by an abrupt increase in tree pollen and a decline in steppe vegetation (Andreev et al., 1997; Fradkina et al., 2005; Andreev and Tarasov, 2013). During the Allerød Interstadial the average temperatures first rose, then fell again during the Younger Dryas (YD; Andreev et al., 2012). During the YD (between about 13,000 – 11,500 cal. yrs. BP), precipitation was about 150 mm per year lower than today (Andreev et al., 1997; Andreev and Tarasov, 2013). A cold, dry phase during the YD was assumed as well by Biskaborn et al. (2012) for eastern Siberia; as they discussed, the resulting prolonged winter ice layer on thermokarst lakes caused reducing water conditions. Nazarova et al. (2013) show that colder conditions than today existed between 10,000 and 8000 cal. yrs. BP, but they assume wet summers also.

Although clear evidence of the thermokarst initiation timing could not be deduced from the studied sediments, we interpret the different biogeochemical characteristics of the lower basin center core parts (>Fe/Mn, >S, >CaCO3) as indicators for initial thermokarst processes (i.e. surface subsidence, ponding water; e.g. Bouchard et al., 2011; Biskaborn et al., 2013b; Schleusner et al., 2015; Figs. 6 and 7). The evolution of both studied thermokarst basins likely began at the KB3, YU2, and YU3 core locations (Fig. 12a). The late Pleistocene ages at the bottom of these sediment sequences does not show the "true" deposition age but rather indicate in situ thaw and subsequent Yedoma deposit subsidence (Tab. 1). The low TOC level in the KB3, YU2, and YU3 basin center cores also suggests further organic matter decomposition within a talik below the developing thermokarst lakes as described from taberal deposits found below Yedoma thermokarst lakes elsewhere (Schirrmeister et al., 2011a; Wetterich et al., 2012; Farquharson et al., 2016). The rEMs also show continuous low-energy deposition, a conclusion mainly supported by a strong influence of rEM1 and rEM2. However, the base of the thermokarst deposits was probably not drilled, as no grain size changes were found indicating the somewhat sandier facies typical for CY Yedoma deposits (Windirsch, 2018).

5.4.2 Holocene thermal maximum thermokarst intensification

Our results show high sedimentation rates and increased bioproductivity in the thermokarst deposits during the mid-HTM (about 7000 - 5000 cal. yrs. BP). This is especially evident by higher organic carbon contents and decreasing $\delta^{13}C$ values in the KB7 core. In addition the YU1 profile, for example, shows increased TOC contents and strong sediment rearrangements during the middle Holocene. The exceptionally high KB7 core sedimentation rates in addition to lacustrine microfossil and palynological data analyses are interpreted by Ulrich et al. (2017b) to indicate rapid, highly dynamic lake evolution during the HTM. In particular, analysis of changes in the species composition of subfossil cladoceras communities made it possible to identify a rapid initiation, growth, and disappearance of an individual thermokarst lake at the KB7 location (Frolova et al., 2017; Ulrich et al., 2017b). Permafrost thaw and extensive thermokarst basin development was probably accelerated especially by rising precipitation (Monserud et al., 1998; Fradkina et al., 2005; Grosse et al., 2013; Nazarova et al., 2013).

Terrestrial conditions changed quickly to lacustrine conditions, and thermokarst lakes rapidly emerged and grew larger in a very short time before thermokarst processes declined locally (Fig. 12b). The same can be seen in the KB6 sediment sequence of the small neighboring basin at the KB study site. The grain-size means are higher in the lower and upper core parts but show a significant increase of finer grain sizes (silt and clay) in the middle part. This change is also reflected in the biogeochemical properties. However, the exact timing of lake drainage to the KB basin is uncertain. The sedimentological and biogeochemical parameters from the upper core indicate changing phases of higher and lower lateral erosion and changing lake levels. A piece of wood sampled from about 90 cm bs was dated to 3316±61 cal. yrs. BP and originated from a short, stable, but rather shallow lake phase (Fig. 3; Tab. 1). The basin center core locations were probably already in a distal position to the lake shore as indicated by homogeneous fine-grained sedimentation. However, the fluctuations in the Fe/Mn and Mg/Ca ratios indicate changing redox conditions during lake level changes.

The HTM is characterized by rising temperatures and higher precipitation in CY (Fradkina et al., 2005; Nazarova et al., 2013). According to Monserud et al. (1998), winter temperatures in Siberia were about 3.7°C and July means about 0.7°C warmer than today and annual rainfall was about 154 mm higher than today. Postglacial warming reached its maximum between about 6000 and 4600 cal. yrs. BP and was characterized by a similar vegetation composition as we see today in Siberia (Monserud et al., 1998). Biskaborn et al. (2012) suggest the warmest period of the mid-Holocene occurred between 7100 and 2800 cal. yrs. BP. At the HTM end, the unification of large thermokarst lake basins took place and alases appeared as they do today. The large pingos in the KB basin are an indication of that. Considering very slow pingo growth rates of a few millimeters per year (Soloviev, 1973), the existence of ⩽12-m-high pingos proves that permafrost aggradation and talik refreezing must have started at that time. Furthermore, the lenticular-layered to reticulate cryostructures as described from the basal parts of the sediment sequences (Fig. 4), in particular from the KB alas, indicate the vertical refreezing of subaqueous water-saturated talik deposits during lake disappearance (Katasonov and Ivanov, 1973; French and Shur, 2010).

Macro remain dating of the upper YU1 profile shows an age of 4606±175 cal. yrs. BP and indicates strong sediment rearrangement during the decaying HTM, likely by thermoerosional processes at a lake basin shore. The uppermost sediments of the YU3 basin center core instead reveal a macro remain date of 3975±102 cal. yrs. BP and subaquatic to subaerial conditions at that time.

5.4.3 Late Holocene thermokarst cessation

Temperatures in eastern Siberia declined again after 4800 to 4500 cal. yrs. BP with minima between 3000 and 2000 cal. yrs. BP (Biskaborn et al., 2012; Nazarova et al., 2013). This was followed by a general warming trend and especially increasing winter temperatures in Siberia but also more short-term temperature fluctuations (Meyer et al., 2015). Sedimentary conditions are generally characterized by low carbon content, higher TOC/TN ratios, and low sedimentation rates, all suggesting a general surface stability and permafrost aggradation below large thermokarst basins during the late Holocene, However, very short favorable periods probably led to higher lake levels and increasing thermoerosional processes at the basin edges. In particular, the KB1 profile shows strong sediment rearrangements under subaquatic conditions, likely via lake shore erosion and slumping processes between 1930±57 and 1812±72 cal. yrs. BP. The higher sand content within the KB1 sediment sequence, the very poor sorting of the grain sizes, and the multiple inversions of the radiocarbon dates indicate high geomorphic dynamics at the basin edge. The rEM scores of the KB1 profile also show this trend towards higher proportions of coarser grain sizes. The biogeochemical records like the low TOC and S values as well as high, varying TOC/TN, Mg/Ca, and Fe/Mn ratios suggest low bioproductivity during sediment repositioning and accumulation and indicate increasing subaerial conditions under short-term changing environmental conditions (Fig. 12c) (Biskaborn et al., 2013b). Strong single events, e.g. collapsing lake-shore bluffs during lake expansion, are an explanantion for the high sedimentation rates and comparable sedimentary conditions (Biskaborn et al., 2013b; Lenz et al., 2013; Séjourné et al., 2015). However, we cannot directly demonstrate comparable high geomorphologic dynamics in the YU thermokarst basin for the same time period. Thus, a regional climate-relevant signal from late Holocene sediment rearrangements as seen in the KB1 core cannot be detected. Our data point to the cessation of thermokarst activity and extensive frost-induced processes (i.e. permafrost aggradation) for the time after about 1.5 cal kyrs BP. Kachurin (1962) suggested that thermokarst processes in Siberia were generally weaker during the late Holocene period. This is generally confirmed by a late Holocene cooling trend, which is frequently observed from lake sediments in northeastern Siberia (Popp et al., 2006; Swann et al., 2010; Biskaborn et al., 2012, 2013a; Klemm et al., 2016).

5.4.4 Recent to modern renewed thermokarst dynamics

Satellite images from the YU basin show different elevated ground levels of the alas bottom around the YU3 and YU1 core locations, which are characterized by drier vegetation conditions (Figs. 2 and 3; see also Ulrich et al., 2017a and their Fig. 2). Different basin ground levels likely indicate small-scale differences in the ground-ice content of the underlying Yedoma deposits and/or differing strong subsidence of the surface and lake deepening (e.g. Morgenstern et al., 2013). They probably also mark the former remnants of Yedoma uplands, which have separated several small thermokarst lakes basin before (Fig. 12b). However, the exact time of small lakes coalescing into a larger lake cannot be determined on the basis of the available data. Also, we believe that coalescence was more of a successive process, in which a lake with a higher water level drained into another when the Yedoma bridge between them was sufficiently thawed and eroded. The same is observed today at the YU study site, as the example of the YU5 location shows. This lake drained into the YU alas in spring 2007 after very rainy years (Ulrich et al., 2017a).

Contemporary northern latitude warming has been confirmed in numerous studies and it is generally known that related environmental changes in the high, northern latitudes and permafrost landscapes can occur very quickly (Serreze et al., 2000; Serreze and Barry, 2011; Grosse et al., 2016; Walter-Anthony et al., 2018). After about 1500 cal. yrs. BP and a relatively long period of relatively stabile, inactive thermokarst processes (Fig. 12d; e.g., Kachurin, 1962), the gradual warming of permafrost over recent decades in Siberia has led to profound changes in the ecosystem (Fedorov et al., 2014a; Iijima et al., 2016). In CY, the rise in temperature in addition to human impacts is leading to renewed high rates of subsidence and abrupt, rapid thermokarst processes (Brouchkov et al., 2004; Fedorov and Konstantinov, 2009; Fedorov et al., 2014b; Ulrich et al., 2017a). The thermokarst landscape in CY is characterized by a long history of human land use (settlements, agriculture, horse and cattle breeding) since the settling/colonization by the Yakut (Sakha) during the 13th century; these activities occurred on the alases, influenced by thaw lake dynamics (Crate et al., 2017). Above all, the YU5 sediment sequence from the neighboring small basin at the YU study site documents very well this subrecent time period. During the short life of the thermokarst lake which developed in a former agricultural area, strong surface subsidence and lateral lake basin expansion took place (Ulrich et al., 2017a). However, we identified very little accumulation of lacustrine sediments . Thus, we expect very low sedimentation rates in modern rapidly growing thermokarst lakes. Finally, this shows that rapid thermokarst processes can happen during even short-term warm climate conditions. This is proved for the past, is still comprehensible today in many permafrost areas and, above all, is accelerated by human land use in CY.

6 Conclusion

Our study emphasizes that alas and thermokarst lake evolution in CY Yedoma landscapes were not a continuous process during the Late Glacial to Holocene period. Short-term phases of forcing climatic conditions have led to very active thermokarst processes and rapid but locally variable landscape modification. Similar processes are observed in the study region under current climatic changes.

Specific sedimentological and biogeochemical thermokarst deposit characteristics allow the reconstruction of erosion, transport, and sedimentation conditions. In particular, the GSD unmixing procedure of the rEMMA offered us a unique and robust method to detect specific grain-size fractionation and depositional processes during thermokarst development. This is not possible by simple ordination methods (e.g., PCA) that usually cannot handle multimodal data and require data linearity or by manual evaluation of the polymodal GSDs from the rearranged polygenetic Yedoma source sediments. The biogeochemical parameters are statistically separated into organic-dominated (e.g., TOC, TOC/TN, S, Mg/Ca) and inorganic-dominated processes (e.g., $CaCO_3$, Fe/S, δ13C). However, their general weak correlation to the sedimentological characteristics represented by the four final rEMs are suggesting post-sedimentary biogeochemical conditions, lake level changes, and varying organic input.

Considering the rather low time resolution of our study as well as the discussed difficulties in dating of thermokarst sediments and the small-scale sedimentation differences, the results of the radiocarbon dating confirm an extensive deposition of reworked late Pleistocene Yedoma source sediments in peripheral basin zones during thermokarst lake growth. The basin centers are characterized by in situ thaw and subsidence of late Pleistocene sediments during early thermokarst evolution phases, but the subsequent accumulation of clayey and fine silt sediments is assigned to a distal transport or a low-energy sedimentation milieu under increasing lacustrine conditions. Finally, the synopsis of rEMMA and all analyzed proxies in relation to the geomorphological location of the cores reveals small-scale variability of sediment origin in each CY alas. Individual small-scale varying depositional environments of many rapidly growing small thermokarst lakes and basins during the mid-HTM, which finally coalesced, have formed the large thermokarst basins we see today in CY.

Authors contribution

MU conceptualized the project, acquired the funding, collected the profiles, analyzed the data, and wrote the manuscript. HM did the rEMMA, the statistical analysis, and wrote parts of and corrected the manuscript. JoS, CS, LS, and AF assisted during field work, organized field work logistics, did laboratory and data analysis, and/or wrote and corrected parts of the paper. BS did the XRF laboratory analysis and corrected the paper. JeS and CZ have been involved in the study and project design and advanced the manuscript with their ideas.

Data availability

All data for this paper are properly cited and referenced in the reference list. Moreover, data may be available upon request to the corresponding author, or are already available as supplementary data.

Conflict of interest

The authors declare that they have no conflict of interest.

Acknowledgements

We greatly appreciate the efforts of all Russian and German colleagues in organizing and supporting the field work and lab analyses. We thank in particular Alexey R. Desyatkin, Avksenty Kondakov, and Peter V. Efremov for field and drilling assistance and Katja Pöhlmann for laboratory assistance. The paper benefited by English proof-reading and valuable comments from Candace S. O’Connor (Scientific Editor, Fairbanks, Alaska). We are very thankful for valuable comments and constructive reviews by two anonymous referees.

Funding

MU was supported by the German Research Foundation (DFG Grant No.: UL426/1-1) and the Japan Society for the Promotion of Science (FY2018 JSPS Invitational Fellowship for Research in Japan (Long-term), ID-No. L18558). AF was supported by the Russian Federal for Basic Research (ID-No. 18-45-140046). JeS was supported by the European Research Council (Starting Grant #338335) and the Initiative and Networking Fund of the Helmholtz Association (#ERC-0013). LS and JeS aknowledge the German Federal Ministry of Education and Research (“CarboPerm” (03G0836A) and “KoPF” (03F0764A)).

7 References

Andreev, A.A., Klimanov, V.A., Sulerzhitsky, L.D., 1997. Younger Dryas pollen records from central and southern Yakutia. Quat. Int. 41-42, 111–117.

Andreev, A.A., Schirrmeister, L., Tarasov, P.E., Ganopolski, V., Brovkin, V., Siegert, C., Wetterich, S., Hubberten, H.-W., 2012. Vegetation and climate history in the Laptev Sea region (Arctic Siberia) during Late Quaternary inferred from pollen records. Quat.- Sci. Rev. 30, 2182-2199.

Andreev, A.A, Tarasov, P.E., 2013. Northern Asia. In: Elias, S.A. (ed.) The Encyclopedia of Quaternary Science, vol. 4, Amsterdam: Elsevier, pp. 164-172.

Biskaborn, B.K., Herzschuh, U., Bolshiyanov, D., Savelieva, L., Diekmann, B., 2012. Environmental variability in northeastern Siberia during the last ~13,300 yr inferred from lake diatoms and sediment-geochemical parameters. Palaeogeogr. Palaeoecol. 329-330, 22-36. https://doi.org/10.1016/j.palaeo.2012.02.003.

Biskaborn, B.K., Herzschuh, U., Bolshiyanov, D., Savelieva, L., Zibulski, R., Diekmann, B., 2013a. Late Holocene thermokarst variability inferred from diatoms in a lake sediment record from the Lena Delta, Siberian Arctic. J. Paleolimnol. 49, 155-170.

Biskaborn, B.K., Herzschuh, U., Bolshiyanov, D.Y., Schwamborn, G., Diekmann, B., 2013b. Thermokarst processes and depositional events in a tundra lake, northeastern Siberia. Permafrost Periglacial Processes 24(3), 160–174.

Biskaborn, B.K, Subetto, D.A., Savelieva, L.A., Vakhrameeva, P.S., Hansche, A., Herschuh, U., Klemm, J., Heinecke, L., Pestryakova, L.A., Meyer, H., Kuhn, G., 2016. Late Quaternary vegetation and lake system dynamics in north-eastern Siberia: Implications for seasonal climate variability. Quat. Sci. Rev. 147, 406-421.

Blott, S.J., Pye, K., 2001. GRADISTAT: a grain size distribution and statistics package for the analysis of unconsolidated sediments. Earth Surf. Proc. Land. 26(11), 1237–1248.

Bosikov, N.P., 1998. Wetness variability and dynamics of thermokarst processes in Central Yakutia, in: Proceedings of the 7th International Permafrost Conference, June 23-27, 1998, Yellowknife, Canada, Nordicana 57, 71-74.

Bouchard, F., Francus, P., Pienitz, R., Laurion, I., 2011. Sedimentology and geochemistry of thermokarst ponds in discontinuous permafrost, subarctic Quebec, Canada. J. Geophys. Res., 116. G00M04. doi: 10.1029/2011JG001675.

Bouchard, F., Pienitz, R., Ortiz, J.D., Francus, P., Laurion, I., 2013. Palaeolimnological conditions inferred from fossil diatom assemblages and derivative spectral properties of sediments in thermokarst ponds of subarctic Quebec, Canada. Boreas 42(3), 575–595.

Bouchard, F., Francus, P., Pienitz, R., Laurion, I., Feyte, S., 2014. Subarctic thermokarst ponds: Investigating recent landscape evolution and sediment dynamics in thawed permafrost of northern Québec (Canada). Arct. Antarct. Alp. Res. 46(1), 251–271.

Bouchard, F., MacDonald, L.A., Turner, K.W., Thienpont, J.R., Medeiros, A.S., Biskaborn, B.K., Korosi, J., Hall, R.I., Pienitz, R., Wolfe, B.B., 2017. Paleolimnology of thermokarst lakes: a window into permafrost landscape evolution. Arct. Sci. 3, 91–117.

Brouchkov, A., Fukuda, M., Fedorov, A., Konstantinov, P., Iwahana, G., 2004. Thermokarst as a short-term permafrost disturbance, Central Yakutia. Permafrost Periglac. 15, 81-87.

Brown J., Ferrians, Jr. O.J., Heginbottom, J.A., Melnikov, E.S., 2002. Circum-Arctic Map of Permafrost and Ground-Ice Conditions, Version 2. National Snow and Ice Data Center, Boulder: Colorado, USA.

Crate, S., Ulrich, M., Habeck, J.O., Desyatkin, A.R., Desyatkin, R.V., Fedorov, A.N., Hiyama, T., Iijima, Y., Ksenofontov, S., Mészáros, C., Takakura, H., 2017. Permafrost livelihoods: A transdisciplinary review and analysis of thermokarst-based systems of indigenous land use. Anthropocene 18, 89-104.

Czudek, T., Demek, J., 1970. Thermokarst in Siberia and its influence on the development of lowland relief. Quat. Res. 1, 103-120.

Davison, W., 1993. Iron and manganese in lakes. Earth-Sci. Rev. 34(2), 119–163.

Desyatkin, R.V., 2008. Soil formation in thermokarst depressions - Alases of cryolithozone, Novosibirsk “Nauka”. (in Russian)

Dietze, E., Hartmann, K., Diekmann, B., IJmker, J., Lehmkuhl, F., Opitz, S., Stauch, G., Wünnemann, B., Borchers, A., 2012. An end-member algorithm for deciphering modern detrital processes from lake sediments of Lake Donggi Cona, NE Tibetan Plateau, China. Sediment. Geol. 243-244, 169–180.

Dietze, E., Maussion, F., Ahlborn, M., Diekmann, B., Hartmann, K., Henkel, K., Kasper, T., Lockot, G., Opitz, S., Haberzettl, T., 2014. Sediment transport processes across the Tibetan Plateau inferred from robust grain-size end members in lake sediments. Clim. Past 10(1), 91–106.

Dietze, E, Dietze, M., 2019. Grain-size distribution unmixing using the R package EMMAgeo. E&G Quarternary Sci. J., 68, 29-46.

Dietze, M., Dietze, E., Lomax, J., Fuchs, M., Kleber, A., Wells, S., 2016. Environmental history recorded in aeolian deposits under stone pavements, Mojave Desert, USA. Quaternary Research, 85(1), 4-16. doi:10.1016/j.yqres.2015.11.007.

Evans, M.E., Heller, F., Bloemendal, J., Thouveny, N., 1997. Natural magnetic archives of past global change. Surv. Geophys. 18, 183-196.

Farquharson, L., Walter Anthony, K., Bigelow, N., Edwards, M., Grosse, G., 2016. Facies analysis of yedoma thermokarst lakes on the northern Seward Peninsula, Alaska. Sediment. Geol. 340, 25-37.

Fedorov, A.N., Konstantinov, P.Y., 2003. Observation of surface dynamics with thermokarst initiation, Yukechi site, CY, in: Permafrost: Proceedings of the 8th International Conference on Permafrost, 21-25 July 2003, pp. 239-243, Zürich, Switzerland.

Fedorov, A.N., Konstantinov, P.Y., 2008. Recent changes in ground temperature and the effect on permafrost landscapes in CY, in: Kane, D.L., Hinkel, K.M. (Eds.), Proceedings of the Ninth International Conference on Permafrost, University of Alaska Fairbanks, June 29–July 3, 2008, Institute of Northern Engineering, University of Alaska, Fairbanks, pp. 433-438.

Fedorov, A.N., Konstantinov P.Y., 2009. Response of permafrost landscapes of Central Yakutia to current changes of climate, and anthropogenic impacts. Geograph. Nat. Resour., 30, 146-150.

Fedorov, A.N., Ivanova, R.N., Park, H., Hiyama, T., Iijima, Y., 2014a. Recent air temperature changes in the permafrost landscapes on northeastern Eurasia. Polar Sci. 8(2), 114–128.

Fedorov, A.N., Gavriliev, P.P., Konstantinov, P.Y., Hiyama, T., Iijima, Y., Iwahana, G., 2014b. Estimating the water balance of a thermokarst lake in the middle of the Lena River basin, eastern Siberia. Ecohydrology 7(2), 188–196.

Flemming, B.W., 2007. The influence of grain-size analysis methods and sediment mixing on curve shapes and textural parameters: Implications for sediment trend analysis. Sediment. Geol. 202(3), 425–435.

Folk, R.L., Ward, W.C., 1957. Brazos River Bar: A study in the significance of grain size parameters. J. Sediment. Petrol. 27(1), 3–26.

Fradkina, A.F., Alekseev, M.N., Andreev, A.A., Klimanov, V.A., 2005. East Siberia. In: Velichko, A.A., Nechaev, V.P. (Eds). Cenozoic Climatic and Environmental Changes in Russia, London, The Geological Society of America (Special Paper 382), pp. 105–120.

French, F., Shur, Y., 2010. The principles in cryostratigraphy. Earth-Sci. Rev. 101, 190-206.

Fritz, M. . Unkel, I., Lenz, J., Gajewski, K, Frenzel, P., Paquette, N., Lantuit, L., Körte, L., Wetterich, S., 2018. Regional environmental change versus local signal preservation in Holocene thermokarst lake sediments: A case study from Herschel Island, Yukon (Canada). J Paleolimnol (2018) 60:77–96. doi.org/10.1007/s10933-018-0025-0

Frolova, L.A., Nazarova, L., Pestryakova, L.A., Herzschuh, U., 2014. Subfossil cladoceran remains from sediment in thermokarst lakes in northeastern Siberia, Russia in relation to limnological and climatic variables. J. Paleolim. 52, 107-119.

Frolova, L.A., Ibragimova, A.G., Ulrich, M., Wetterich, S., 2017. Reconstruction of the history of a thermokarst lake in the Mid-Holocene based on an analysis of subfossil cladocera (Siberia, Central Yakutia). Cont. Probl. Ecol. 10(4), 423-430.

Gaglioti, B.V., Mann, D.H., Jones, B.M., Pohlman, J.W., Kunz, M.L., Wooller, M.J., 2014. Radiocarbon age-offsets in an arctic lake reveal the long-term response of permafrost carbon to climate change. J. Geophys. Res.-Biogeo. 119(8), 1630–1651.

Gavrilova, M.K., 1973. Climate of Central Yakutia. Akademiya Nauk, Institut Merzlotovedeniya, Yakutsk, SSSR, pp 120. (in Russian)

Global Wind Atlas (2018). A free, web-based application developed, owned and operated by the Technical University of Denmark (DTU) in partnership with the World Bank Group, utilizing data provided by Vortex, with funding provided by the Energy Sector Management Assistance Program (ESMAP). https://globalwindatlas.info/ (accessed 9 April 2019).

Grosse, G., Jones, J., Arp, C., 2013. Thermokarst lakes, drainage, and drained basins, in: Shroder, J.F. (Ed.), Treatise on Geomorphology, San Diego, Academic Press, pp. 325-353.

Grosse, G., Goetz, S., McGuire, A.D., Romanovsky, V.E., Schuur, E.A.G., 2016. Changing permafrost in a warming world and feedbacks to the Earth system. Environ. Res. Lett. 11, 040201, doi:10.1088/1748-9326/11/4/040201.

Haberzettl, T., Corbella, H., Fey, M., Janssen, S., Lücke, A., Mayr, C., Ohlendorf, C., Schäbitz, F., Schleser, G.H., Wille, M., Wulf, S., Zolitschka, B., 2007. Lateglacial and Holocene wet–dry cycles in southern Patagonia: chronology, sedimentology and geochemistry of a lacustrine record from Laguna Potrok Aike, Argentina. Holocene 17, 297–310.

Hamann, Y., Ehrmann, W., Schmiedl, G., Krüger, S., Stuut, J.-B., Kuhnt, T., 2008. Sedimentation processes in the Eastern Mediterranean Sea during the Late Glacial and Holocene revealed by endmember modelling of the terrigenous fraction in marine sediments. Mar. Geol. 248(1-2), 97–114.

Hanesch, M., Scholger, R., 2005. The influence of soil type on the magnetic susceptibility measured throughout soil profiles. Geophys. J. Int. 161(1), 50–56.

Hartmann, D., 2007. From reality to model: Operationalism and the value chain of particle-size analysis of natural sediments. Sediment. Geol. 202(3), 383–401.

Iijima, Y., Ohta, T., Kotani, A., Fedorov, A.N., Kodama, Y., Maximov, T.C., 2014. Sap flow changes in relation to permafrost degradation under increasing precipitation in an eastern Siberian larch forest. Ecohydrology 7, 177–187.

Iijima, Y., Nakamura, T., Hotaek, P., Tachibana, Y., Fedorov, A.N., 2016. Enhancement of Arctic storm activity in relation to permafrost degradation in eastern Siberia. Int. J. Clim., 36, 4265–4275.

Ijmker, J., Stauch, G., Dietze, E., Hartmann, K., Diekmann, B., Lockot, G., Opitz, S., Wünnemann, B., Lehmkuhl, F., 2012. Characterisation of transport processes and sedimentary deposits by statistical end-member mixing analysis of terrestrial sediments in the Donggi Cona lake catchment, NE Tibetan Plateau. Sediment. Geol. 281, 166–179.

IPCC (Intergovernmental Panel on Climate Change) 2013, in: Stocker, T.F., Qin, D., Plattner, G.-K., Tignor, M., Allen, S.K., Boschung, J., Nauels, A., Xia, J., Bex, V., Midgley, P.M. (eds), Climate Change 2013: The Physical Science Basis, Contribution Working Group I to the Fifth Assessment Report of the Intergovernmental Panel on Climate Change, Cambridge, Cambridge Univ. Press., pp. 3-29.

Ji, S., Xingqi, L., Sumin, W., Matsumoto, R., 2005. Palaeoclimate changes in the Qinghai Lake area during the last 18,000 years. Quat. Int. 136, 131-140.

Jongejans, L.L., Strauss, J., Lenz, J., Peterse, F., Mangelsdorf, K., Fuchs, M, Grosse, G., 2018. Organic matter characteristics in yedoma and thermokarst deposits on Baldwin Peninsula, west Alaska. Biogeosciences, 15 (2), 6033 – 6048.

Josse, J., Husson, F., 2016. missMDA: A package for handling missing values in multivariate data analysis. Journal of Statistical Software, 70(1), 1-31. doi: 10.18637/jss.v070.i01.

Kachurin, S.P., 1962. Thermokarst within the territory of the USSR. Biuletyn Peryglacjalny, 11, 49–55. (In Russian.)

Katamura, F., Fukuda, M., Bosikov, N.P., Desyatkin, R.V., Nakamura, T., Moriizumi, J., 2006. Thermokarst formation and vegetation dynamics inferred from a palynological study in Central Yakutia, Eastern Siberia, Russia. Arct. Antarct. Alp. 38, 561-570.

Katamura, F., Fukuda, M., Bosikov, N.P., Desyatkin, R.V., 2009. Charcoal records from thermokarst deposits in central Yakutia, eastern Siberia: Implications for forest fire history and thermokarst development. Quat. Res. 71(1), 36–40.

Katasonov, E.M., Ivanov, M.S., 1973. Cryolithology of Central Yakutia: Guidebook, II International Conference on Permafrost, Yakutsk. USSR Academy of Sciences, Siberian Division, Yakutsk, 38 pp.

Katasonov, E.M., Ivanov, M.S., Pudov, G.G., Siegert, C., Katasonova, E.G., 1979. Structure and absolute geochronology of alas deposits in Central Yakutia. Moscow, Nauka. (in Russian).

Klemm, J., Herschuh, U., Pestryakova, L.A., 2016. Vegetation, climate and lake changes over the last 7000 years at the boreal treeline in north-central Siberia. Quat. Sci. Rev. 147, 422-434.

Klovan, J.E., Imbrie, J., 1971. An algorithm and Fortran-IV program for large-scale Q-mode factor analysis and calculation of factor scores. Math. Geol. 3(1), 61–77.

Lenz, J., Fritz, M., Wetterich, S., Schirrmeister, L., Lantuit, H., Wooller, M.J., Pollar, W.H., Wetterich, S., 2013. Periglacial landscape dynamics in the West-Canadian Arctic – Results from a lake record on a push moraine (Herschel Island, Yukon Territory). Palaeogeogr. Palaeoecol. 381-382, 15-25.

Lenz, J., Grosse, G., Jones, B.M., Walter Anthony, K.M., Bobrov, A., Wulf, S., Wetterich, S., 2016. Mid-Wisconsin to Holocene permafrost and landscape dynamics based on a drained lake basin core from the northern Seward Peninsula, Northwest Alaska. Permafr. Periglac. 27(1), 56-75.

Liu, X., Herschuh, U., Shen, J., Jiang, Q., Xiao, X., 2008. Holocene environmental and climatic changes inferred from Wulungu Lake in northern Xinjiang, China. Quat. Res. 70, 412-425.

Macumber, A.L., Patterson, R.T., Galloway, J.M., Falck, H., Swindles, G.T., 2018. Reconstruction of Holocene hydroclimatic variability in subarctic treeline lakes using lake sediment grain-size end-members. The Holocene 28(6), 845–857.

Matasova, G., Petrovský, E., Jordanova, N., Zykina, V., Kapička, A., 2001. Magnetic study of Late Pleistocene loess/palaeosol sections from Siberia: palaeoenvironmental implications. Geophys. J. Int. 147(2), 367– 380.

Melillo, J.M., Aber, J.D., Linkins, A.E., Ricca, A., Fry, B., Nadelhozer, K. J., 1989. Carbon and nitrogen dynamics along the decay continuum: Plant litter to soil organic matter. Plant and Soil, 115, 189–198.

Meyer, H., Opel, T., Laepple, T., Dereviagin, A. Y., Hoffmann, K., Werner, M., 2015. Long-term winter warming trend in the Siberian Arctic during the mid- to late Holocene, Nature Geosci., 8, 122–125.

Meyers, P.A., 1994. Preservation of elemental and isotopic source identification of sedimentary organic matter. Chem. Geol. 114(3-4), 289–302.

Meyers, P.A., Lallier-Vergès, E., 1999. Lacustrine sedimentary organic matter records of Late Quaternary paleoclimates. J. Paleolim. 21, 345–372.

Meyers, P.A., Teranes, J.L., 2001. Sediment organic matter, in: Last, W.M., Smol, J.P. (Eds.), Tracking Environmental Changes Using Lake Sediments—Volume II: Physical and Chemical Techniques. Kluwer, Dordrecht, pp. 239–269.

Mirkin, B.M., Gogoleva, P.A., Kononov, K.E., 1985. The vegetation of Central Yakutian alases. Folia Geobot. Phytotax. 20, 345-395.

Monserud, R.A., Tchebakova, N.M., Denissenko, O.V., 1998. Reconstruction of the mid-Holocene palaeoclimate of Siberia using a bioclimatic vegetation model. Palaeogeogr. Palaeoecol. 139, 15–36.

Morgenstern, A., Grosse, G., Günther, F., Fedorova, I., Schirrmeister, L., 2011. Spatial analyses of thermokarst lakes and basins in Yedoma landscapes of the Lena Delta. The Cryosphere 5, 849-867.

Morgenstern, A., Ulrich, M., Günther, F., Roessler, S., Fedorova, I.V., Rudaya, N.A., Wetterich, S., Boike, J., Schirrmeister, L., 2013. Evolution of thermokarst in East Siberian ice-rich permafrost – a case study. Geomorphology 201, 363-379.

Nazarova, L., Lüpfert, H., Subetto, D., Pestryakova, L.A., Diekmann, B., 2013. Holocene climate conditions in central Yakutia (Eastern Siberia) inferred from sediment composition and fossil chironomids of Lake Temje. Quat. Int. 290-291, 264-274.

Nottebaum, V., Stauch, G., Hartmann, K., Zhang, J., Lehmkuhl, F., 2015. Unmixed loess grain size populations along the northern Qilian Shan (China): Relationships between geomorphologic, sedimentologic and climatic controls. Quat. Int. 372, 151–166.

O'Leary, M.H., 1981. Carbon isotope fractionation in plants. Phytochemistry 20(4), 553– 567.

Olefeldt, D., Goswami, S., Grosse, G., Hayes, D., Hugelius, G., Kuhry, P., McGuire, A. D., Romanovsky, V.E., Sannel, A.B.K., Schuur, E.A.G., Turetsky, M.R., 2016. Circumpolar distribution and carbon storage of thermokarst landscapes. Nat. Commun.7, 13043, doi:10.1038/ncomms13043 (2016)

Opitz, S., Ramisch, A., Mischke, S., Diekmann, B., 2013. Holocene lake stages and thermokarst dynamics in a discontinuous permafrost affected region, north-eastern Tibetan Plateau. J. Asian Earth Sci. 76, 85–94.

Pestryakova, L.A., Herzschuh, U., Wetterich, S., Ulrich, M., 2012. Present-day variability and Holocene dynamics of permafrost-affected lakes in central Yakutia (Eastern Siberia) inferred from diatom records. Quat. Sci. Rev. 51, 56-70.

Popp, S., Diekmann, B., Meyer, H., Siegert, C., Syromyatnikov, I., Hubberten, H.-W., 2006. Palaeoclimate signals as inferred from stable-isotope composition of ground ice in the Verkhoyansk Foreland, Central Yakutia. Permafrost Periglacial Processes 17, 119-132.

Péwé, T.L., Journaux, A., 1983. Origin and character of loess-like silt in unglaciated south-central Yakutia, Siberia, USSR. US Geological Survey Professional Paper 1262.

R Core Team, 2014. R. A language and environment for statistical computing. Version 3.1.1. Wien: R Foundation for Statistical Computing. Online available: http://www.R-project. org/.

Reimer, P., Bard, E., Bayliss, A., Beck, J., Blackwell, P., Ramsey, C., Buck, C.E., Cheng, H., Edwards, R.L., Friedrich, M., Grootes, P.M., Guilderson, T.P., Haflidason, H., Hajdas, I., Hatté, C., Heaton, T.J., Hoffmann, D.L., Hogg, A.G., Hughen, K.A., Kaiser, K.F., Kromer, B., Manning, S.W., Niu, M., Reimer, R.W., Richards, D.A., Scott, E.M., Southon, J.R., Staff, R.A., Turney, C.S.M., Van der Plicht, J., 2013. IntCal13 and Marine13 Radiocarbon Age Calibration Curves 0–50,000 Years cal BP. Radiocarbon 55(4), 1869-1887.

Santoro, M., Strozzi, T., 2012. Circumpolar digital elevation models > 55° N with links to geotiff images. doi:10.1594/PANGAEA.779748.

Schirrmeister, L., Kunitsky, V., Grosse, G., Wetterich, S., Meyer, H., Schwamborn, G., Babiy, O., Derevyagin, A., Siegert, C., 2011a. Sedimentary characteristics and origin of the Late Pleistocene Ice Complex on north-east Siberian Arctic coastal lowlands and islands – A review. Quat. Int. 241(1-2), 3–25. http://doi:10.1016/j.quaint.2010.04.004.

Schirrmeister, L., Grosse, G., Schnelle, M., Fuchs, M., Krbetschek, M., Ulrich, M., Kunitsky, V., Grigoriev, M., Andreev, A., Kienast, F., Meyer, H., Babiy, O., Klimova, I., Bobrov, A., Wetterrich, S., Schwamborn, G., 2011b. Late Quaternary paleoenvironmental records from the western Lena Delta, Arctic Siberia. Palaeogeogr. Palaeoecol. 299(1-2), 175–196. doi: 10.1016/j.quascirev.2009.11.017.

Schirrmeister, L., Grosse, G., Wetterich, S., Overduin, P.P., Strauss, J., Schuur, E.A.G., Hubberten, H.-W., 2011c. Fossil organic matter characteristics in permafrost deposits of the northeast Siberian Arctic. J. Geophys. Res. 116. DOI: 10.1029/2011JG001647.

Schirrmeister, L., Froese, D., Tumskoy, V., Grosse, G., Wetterich, S., 2013. Yedoma: Late Pleistocene ice-rich syngenetic permafrost of Beringia, in: Elias S.A. (ed.), The Encyclopedia of Quaternary Science 2nd edition, vol. 3, Amsterdam, Elsevier, pp. 542-552.

Schirrmeister, L., Schwamborn, G., Overduin, P.P., Strauss, J., Fuchs, M.C., Grigoriev, M., Yakshina, I., Rethemeyer, J., Dietze, E., Wetterich, S., 2017. Yedoma ice complex of the Buor Khaya Peninsula (southern Laptev Sea). Biogeosciences 14, 1261-1283. doi:10.5194/bg-14-1261-2017

Schleusner, P., Biskaborn, B.K., Kienast, F., Wolter, J., Subetto, D., Diekmann, B., 2015. Basin evolution and palaeoenvironmental variability of the thermokarst lake El'gene-Kyuele, Arctic Siberia. Boreas 44, 216-229.

Séjourné, A., Costard, F., Fedorov, A.N., Gargani, J., Skorve, J., Massé, M., Mège, D., 2015. Evolution of the banks of thermokarst lakes in Central Yakutia (Central Siberia) due to retrogressive thaw slump activity controlled by insolation. Geomorphology 241, 31-40.

Serreze, M.C., Walsh, J.E., Chapin III, F.S., Osterkamp, T., Dyugerov, M., Romanovsky, V.E., Oechel, W.C., Morison, J., Zhang, T., Barry, R.G., 2000. Observational evidence of recent change in the northern high-latitude environment. Clim. Change 46, 159–207.

Serreze, M.C., Barry, R.G., 2011. Processes and impacts of Arctic amplification: A research synthesis. Glob. Planet. Change 77, 85–96.

Siegert, C., 1979. Minerologic-petrographic characteristic of alas deposits. in: Katasonov, E.M. (Ed.), Structure and absolute geochronology of alas deposits in Central Yakutia, Moscow, Nauka, pp. 44-61. (In Russian).

Siegert, C., 1987. Greigite and Mackinawite in Quaternary deposits of Central Yakutia. Mineralogicheskiy Zhurnal 9(5), 75-81. (In Russian).

Soloviev, P.A., 1959. Cryolithic zone of the northern part of Lena-Amga interfluve. Moscow, Izdatel'stvo Akademii SSSR, pp. 142. (in Russian).

Soloviev, P.A., 1973. Thermokarst phenomena and landforms due to frost heaving in Central Yakutia. Biuletyn Peryglacjalny 23, 135–155.

Stendel, M., Christensen, J.H., 2002. Impact of global warming on permafrost conditions in a coupled GCM. Geophys. Res. Lett. 29(13), DOI: 10.1029/2001GL014345.

Strauss, J., Schirrmeister, L., Wetterich, S., Borchers, A, Davydov S.P., 2012. Grain-size properties and organic-carbon stock of Yedoma Ice Complex permafrost from the Kolyma lowland, northeastern Siberia. Global Biogeochem. Cy. 26, GB3003. doi:10.1029/2011GB004104.

Strauss, J., Schirrmeister, L., Grosse, G., Wetterich, S., Ulrich, M., Herzschuh, U., Hubberten, H.-W., 2013. The deep permafrost carbon pool of the Yedoma region in Siberia and Alaska. Geophys. Res. Lett. 40, 6165–6170. doi:10.1002/2013GL058088.

Strauss, J., Schirrmeister, L., Mangelsdorf, K., Eichhorn, L., Wetterich, S., Herzschuh, U., 2015. Organic-matter quality of deep permafrost carbon – a study from Arctic Siberia. Biogeosciences, 12(7), 2227-2245. doi:10.5194/bg-12-2227-2015.

Strauss, J., Schirrmeister, L., Grosse, G., Fortier, D., Hugelius, G., Knoblauch, C., Romanovsky, V., Schädel, C., Schneider von Deimling, T., Schuur, E.A.G., Shmelev, D., Ulrich, M., Veremeeva, A., 2017. Deep Yedoma permafrost: A synthesis of depositional characteristics and carbon vulnerability. Earth-Sci. Rev. 172, 75-86. doi: 10.1016/j.earscirev.2017.07.007.

Stuiver, M., Polach, H.A., 1977. Discussion: Reporting of 14C Data. Radiocarbon 19(3), 355–363.

Swann, G.E., Leng, M.J., Juschus, O., Melles, M., Brigham-Grette, J., Sloane, H.J., 2010. A combined oxygen and silicon diatom isotope record of Late Quaternary change in Lake El'gygytgyn, North East Siberia, Quat. Sci. Rev. 29 (5-6), 2010, 774-786.

Tomirdiaro, S.V., 1982. Evolution of Lowland Landscapes in Northeastern Asia during Late Quaternary Time. Paleoecol. Beringia, 29–42.

Ulrich, M., Matthes, H., Schirrmeister, L., Schütze, J., Park, H., Iijima, Y., Fedorov, A.N., 2017a. Differences in behavior and distribution of permafrost-related lakes in Central Yakutia and their response to climatic drivers. Water Resour. Res. 53(2), 1167-1188.

Ulrich, M., Wetterich, S., Rudaya, N., Frolova, L., Schmidt, J., Siegert, C., Fedorov, A.N., Zielhofer, C., 2017b. Rapid thermokarst evolution during the mid-Holocene in Central Yakutia, Russia. The Holocene 27(12), 1899-1913.

Veganzones, M.A., Grana, M., 2008. Endmember extraction methods: A short review, in: Lovrek, I., Howlett, R.J., Jain, L.C. (Eds.). KES 2008, Part III, LNAI 5179. Berlin, Heidelberg: Springer, pp. 400–407.

Walter, K.M., Edwards, M.E., Grosse, G., Zimov, S.A., Chapin III, F.S., 2007. Thermokarst lakes as a source of atmospheric CH4 during the last deglaciation. Science 318, 633-636.

Walter Anthony, K.M., Zimov, S.A., Grosse, G., Jones, M.C., Anthony, P.M., Chapin III, F.S., Finlay, J.C., Mack, M.C., Davydov, S., Frenzel, P., Frolking, S., 2014. A shift of thermokarst lakes from carbon sources to sinks during the Holocene epoch. Nature, 511, 452–456.

Walter Anthony, K., Schneider von Deimling, T., Nitze, I., Frolking, S., Emond, A., Daanen, R., Anthony, P., Lindgren, P., Jones, B., Grosse, G., 2018. 21st-century modeled permafrost carbon emissions accelerated by abrupt thaw beneath lakes. Nature Com., 9:3262. DOI:10.1038/s41467-018-05738-9.

Weltje, G.J., Prins, M.A., 2003. Muddled or mixed? Inferring palaeoclimate from size distributions of deep-sea clastics. Sediment. Geol. 162(1-2), 39–62.

Weltje, G.J., Prins, M.A., 2007, Genetically meaningful decomposition of grain-size distributions. Sediment. Geol. 202(3), 409– 424.

Wetterich, S.. Schirrmeister, L., Pietrzeniuk, E., 2005. Freshwater ostracodes in Quaternary permafrost deposits in the Siberian Arctic. J Paleolim. 34(3), 363–376.

Wetterich, S., Schirrmeister, L., Meyer, H., Siegert, C., 2008. Thermokarst lakes in Central Yakutia (Siberia) as habitats of freshwater ostracodes and archives of palaeoclimate, in: Kane, D.L., Hinkel, K.M. (Eds.), Ninth International Conference on Permafrost, University of Alaska Fairbanks, Institute of Northern Engineering, pp. 1945-1950.

Wetterich, S., Grosse, G., Schirrmeister, L., Andreev, A.A., Bobrov, A.A., Kienast, F., Bigelow, N.H., Edwards, M.E., 2012. Late Quaternary environmental and landscape dynamics revealed by a pingo sequence on the northern Seward Peninsula, Alaska. Quat. Sci. Rev. 39, 26–44.

Windirsch, T., 2018. Organic Matter Characteristics in a Changing Permafrost Environment: Yukechi Alas Landscape, Central Yakutia. Master thesis, University of Potsdam, Germany, pp. 39. Online available: http://epic.awi.de/48337/.

Zielhofer, C., Fletcher, W.J., Mischke, S., De Batist, M., Campbell, J.F.E., Joannin, S., Tjallingii, R., El Hamouti, N., Junginger, A., Stele, A., Bussmann, J., Schneider, B., Lauer, T., Spitzer, K., Strupler, M., Brachert, T., Mikdad, A., 2017. Atlantic forcing of Western Mediterranean winter rain minima during the last 12,000 years. Quat. Sci. Rev. 157, 29-51.

Zimov, S.A., Chuprynin, V.I., Oreshko, A.P., Chapin, F.S., Reynolds, J.F., Chapin, M.C., 1995. Steppe-Tundra Transition: A Herbivore-Driven Biome Shift at the End of the Pleistocene. The American Naturalist 146(5), 765-794.

Figures

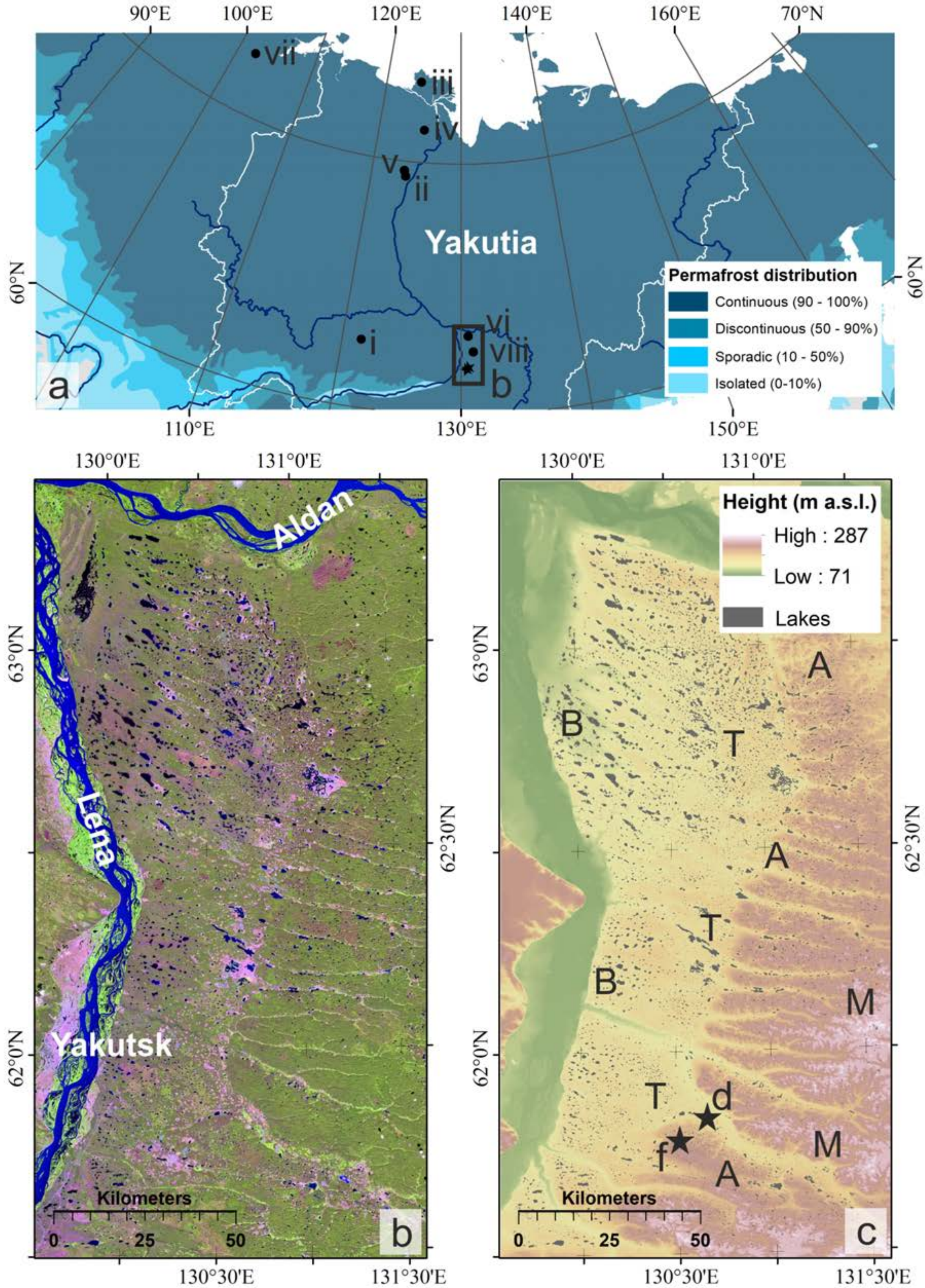

Fig. 1. Study site overview. (a) Location of the study region and the key study sites (black stars) in the zone of continuous permafrost. Roman letters mark previous paleoenvironmental

reconstructions from thermokarst lake sediments in Siberia; i) Andreev et al. (1997), ii) Biskaborn et al. (2012), iii) Biskaborn et al. (2013a), iv) Biskaborn et al. (2013b) / Schleusner et al. (2014), v) Biskaborn et al. (2016), vi) Katamura et al. (2009), vii) Klemm et al., 2016, Popp et al. (2006). Map of permafrost distribution modified after Brown et al. (2002). (b) The Lena-Aldan interfluve region (Landsat 8 closeup, July 2013, USGS). (c) Thermokarst development and lake properties differ on several Pleistocene accumulative-erosive terraces following Soloviev (1959). B: Bestyakh terrace, T: Tyungyulyu terrace, A: Abalakh terrace, M: Magan terrace. In particular the Tyungyulyu and the Abalakh terraces are differentiated due to characteristics and distribution of ice-rich permafrost deposits. The stars are indicating the KB key study site (d) on the Tyungyulyu terrace and the YU key study site (f) on the Abalakh terraces. For details see Figure 2 (DEM generated using data from the ESA DUE Permafrost Project (Santoro and Strozzi, 2012)).

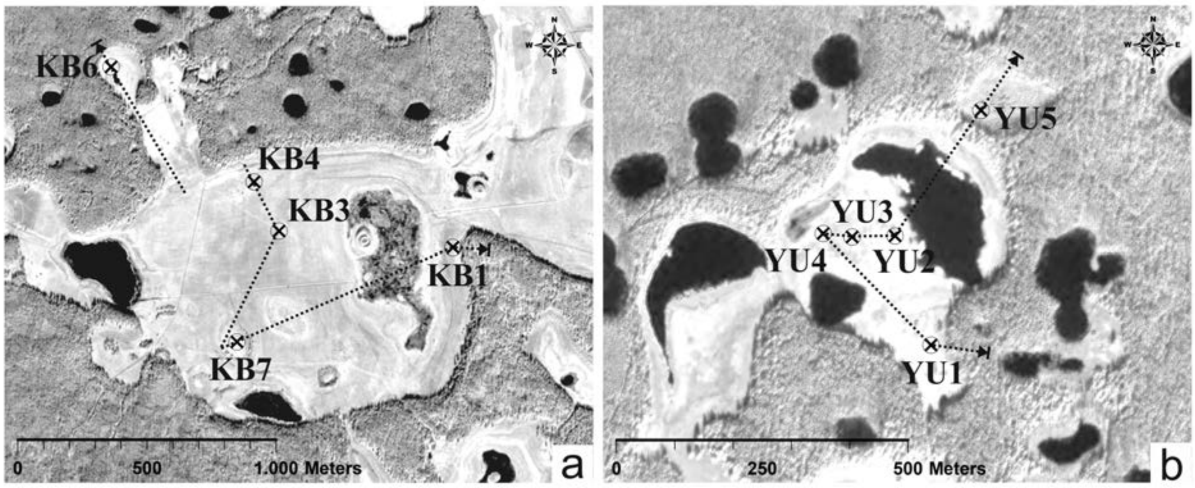

Fig. 2. Satellite images showing the drilling sites within (a) the KB basin and (b) the YU basin (Pleiades-1A subsets, 22 Sept. 2012). The dashed lines mark the topographic profiles illustrated in Fig. 3.

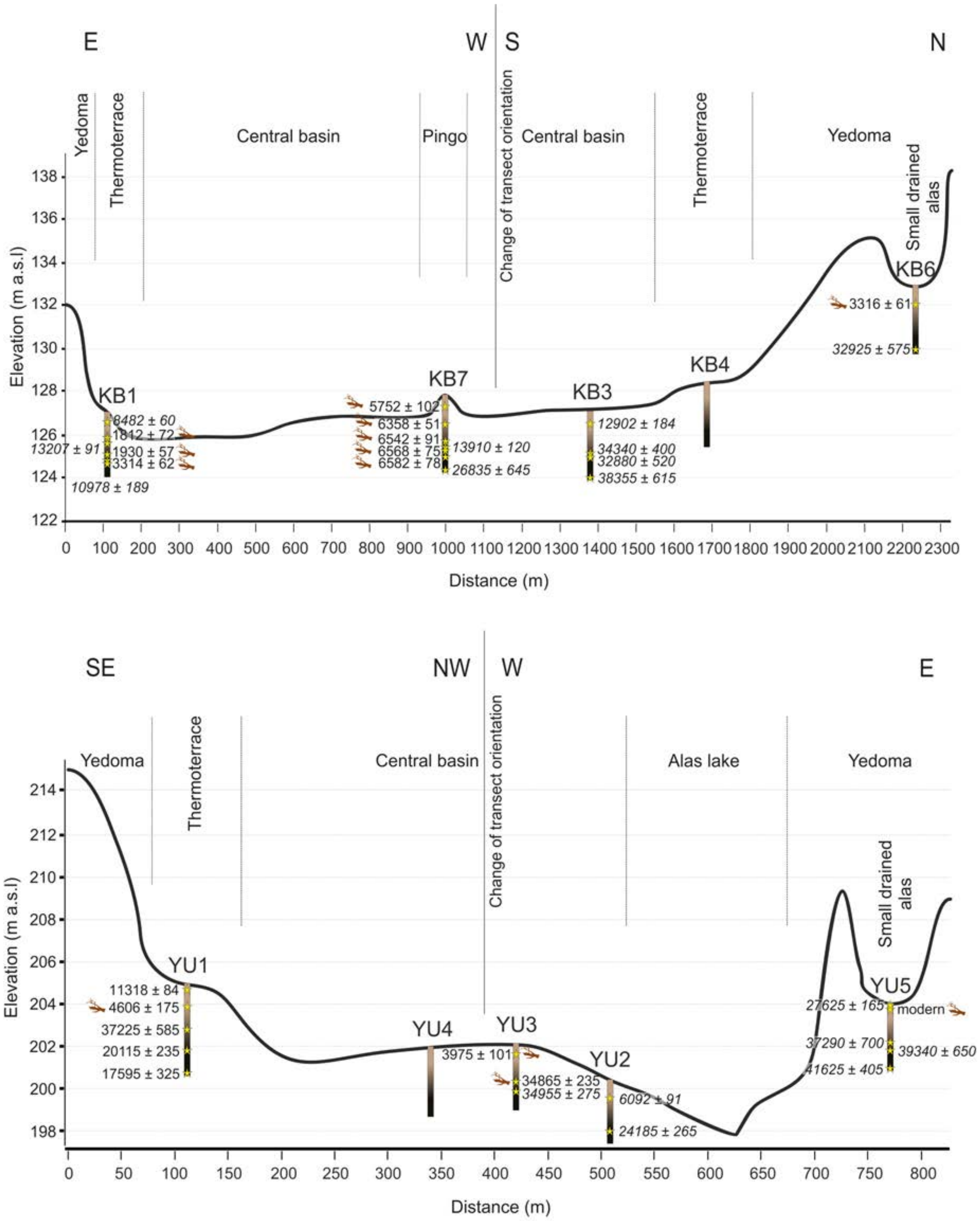

Fig. 3. Coring transects of the studied thermokarst basin in relation to geomorphology and topography. Topographic data based on geodetic field surveys conducted in summer 2014 (see Ulrich et al., 2017a). The radiocarbon dates are shown as cal. yrs. BP for each dated core. The dating of bulk material is highlighted by italics and the macro remains are highlighted by the wooden stick symbols.

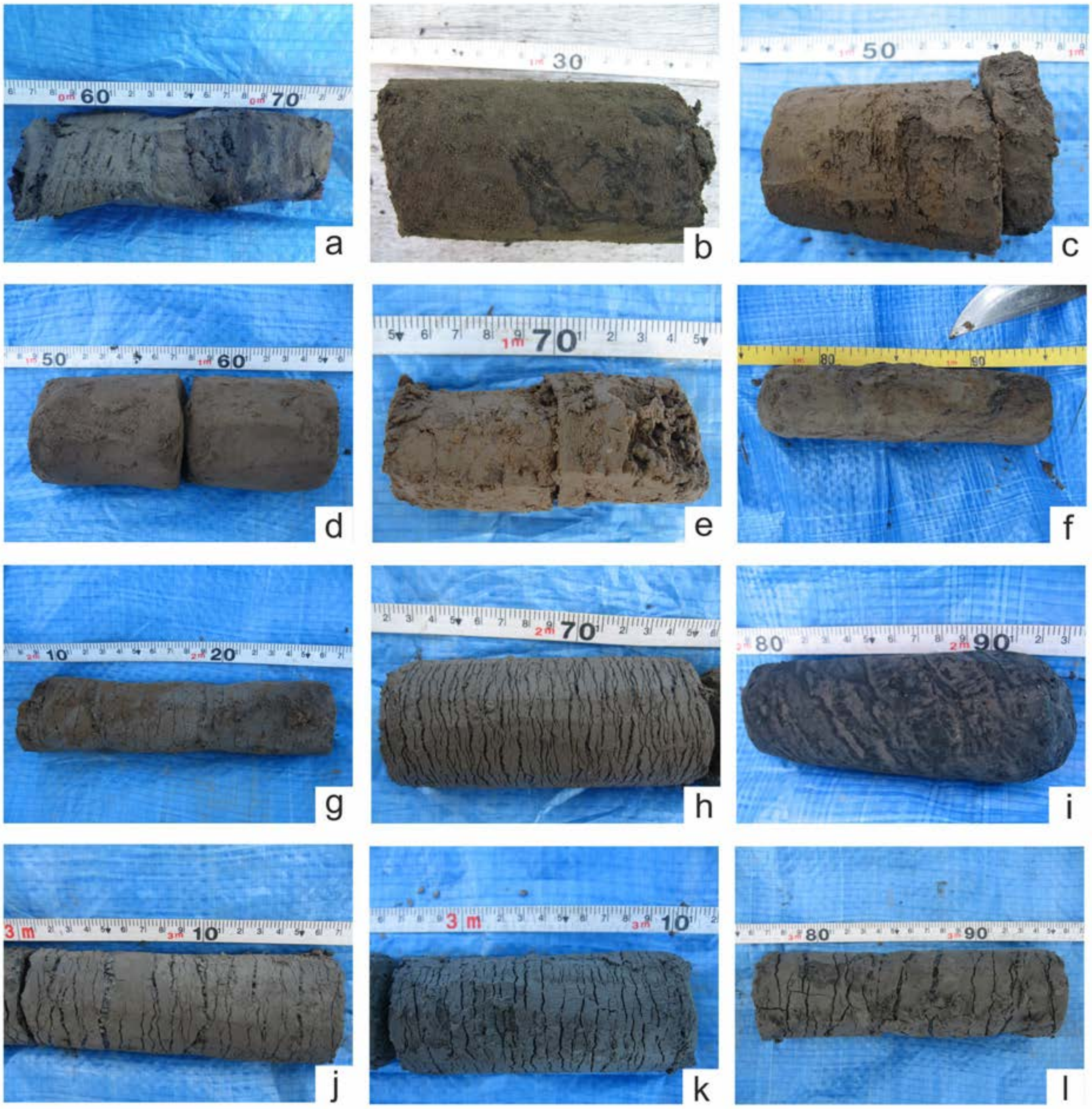

Fig. 4. Example photos of sediment composition, color, and cryolithological properties as seen in the field from the different thermokarst deposit cores. (a) YU2, (b) KB7, (c) KB6, (d) YU5, (e) YU1 (f) KB1, (g) YU3, (h) YU1, (i) KB3, (j) YU1, (k) KB4, (l) YU1. Please see scales for sample depths.

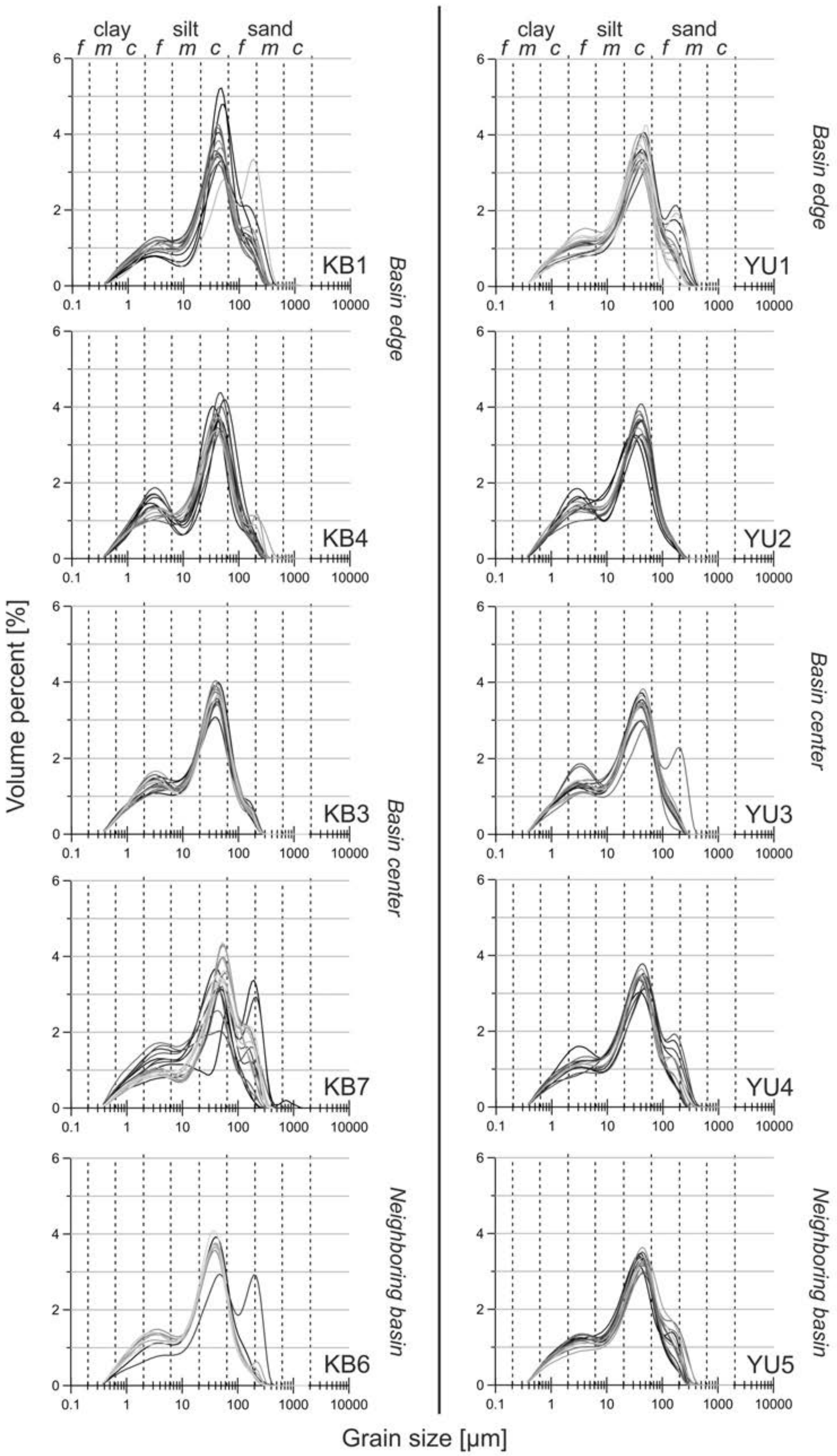

Fig. 5. GSD curves of all thermokarst deposit cores with the KB study site (left) and the YU study site (right). The gray levels of the GSD curves decrease with core depth. Clay, silt, and sand are divided into fine (f), middle (m), and coarse (c) fractions.

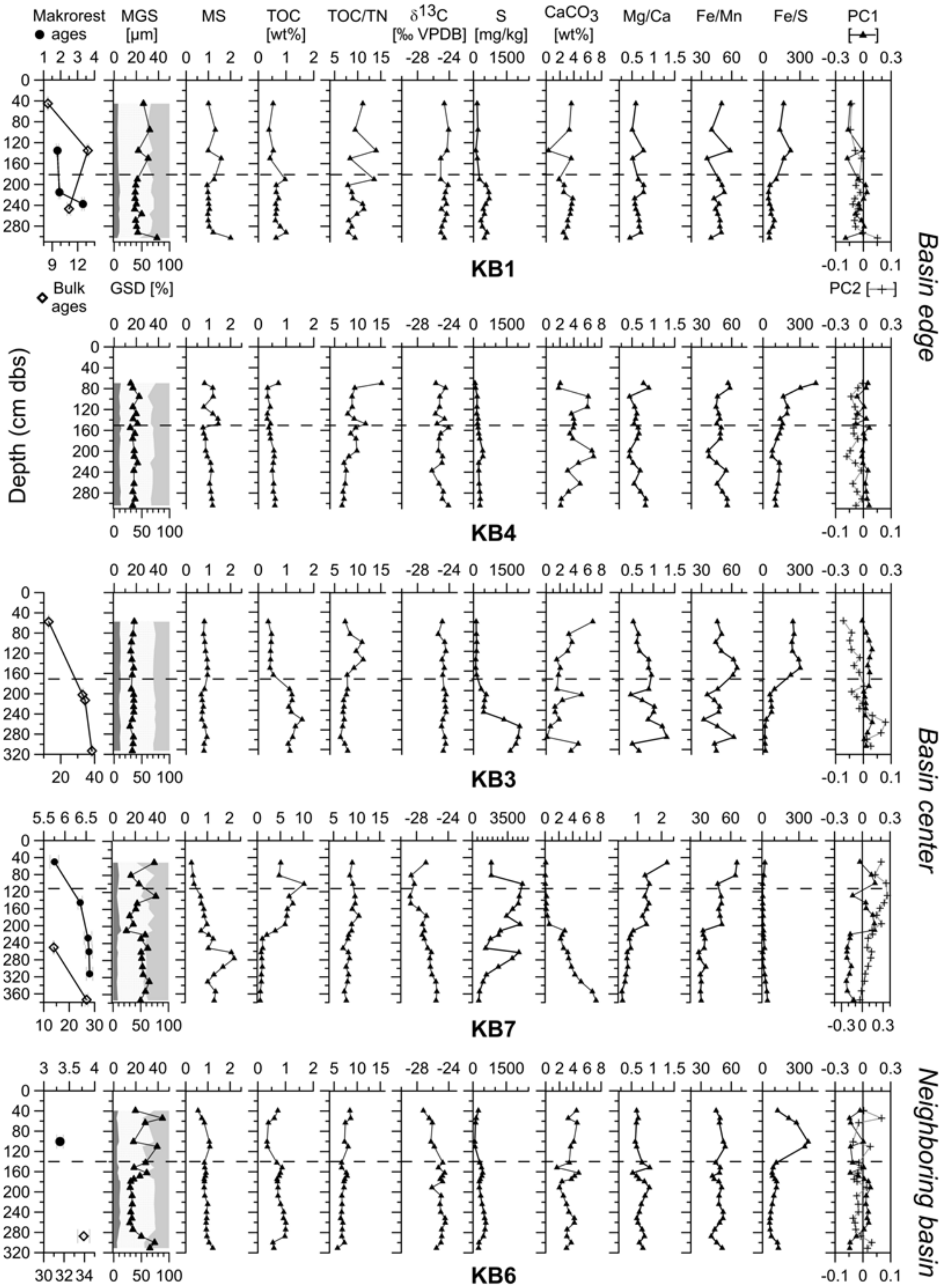

Fig. 6. Sedimentological and biogeochemical results of all KB cores against sample depth with the macro remain and bulk ages in cal. kyrs. BP, the GSD including contents of clay (dark gray), silt (white), sand (light gray) and the grain-size mean as MGS, the MS in SI units (10-6 m3 kg-1), TOC, TOC/TN, δ13C, CaCO3, and selected elements and element ratios from XRF measurements. Additionally, the sample scores on PC1 and PC2 are plotted (See section 4.4). Please note the different scaling of the macro remain and bulk ages as well as TOC, S, and Mg/Ca values and the PC2 scores of KB7. The dashed horizontal lines mark the observed active layer depths.

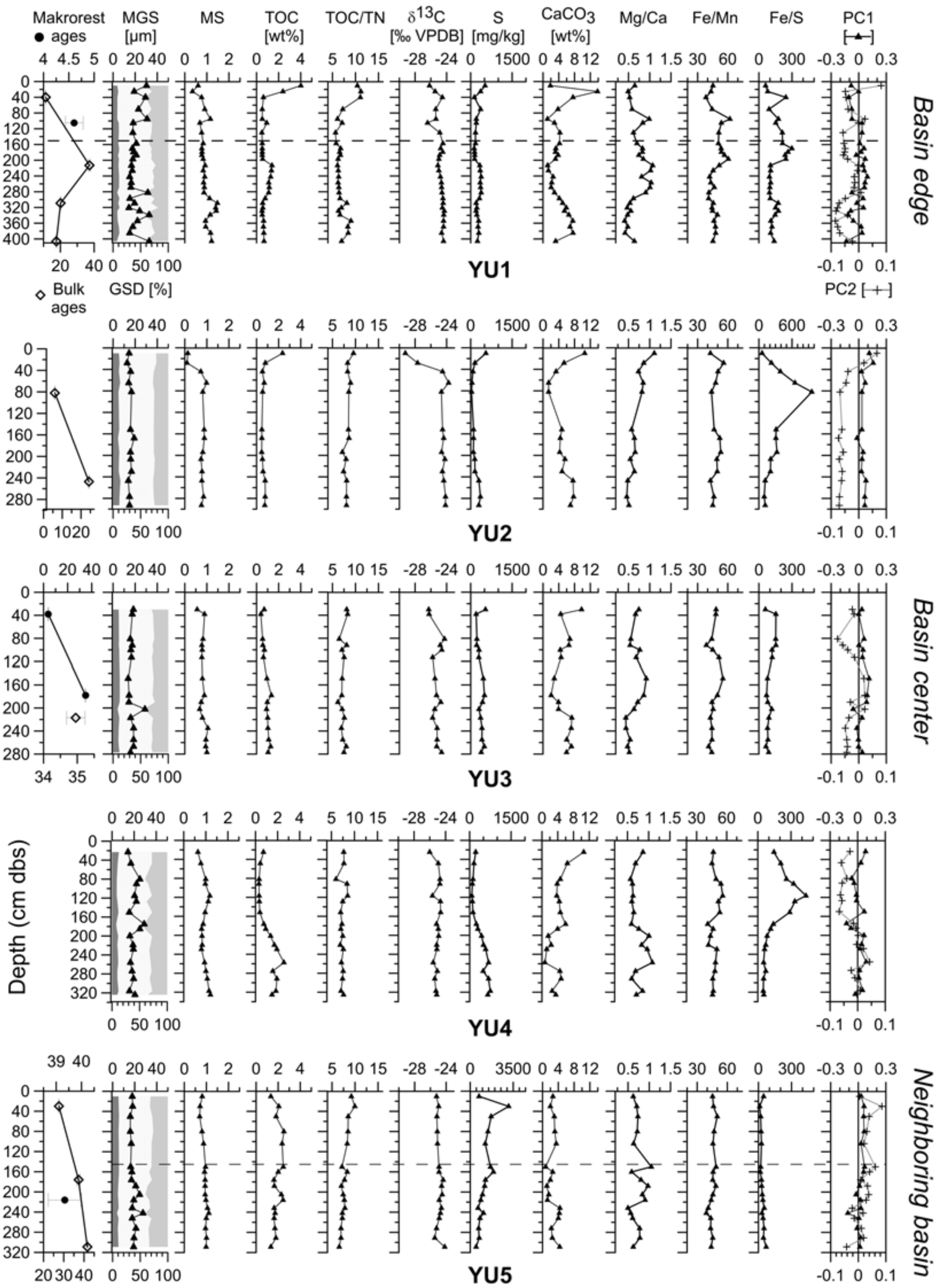

Fig. 7. Sedimentological and biogeochemical results of all YU cores against sample depth with the macro remain and bulk ages in cal. kyrs. BP, the GSD including contents of clay (dark gray), silt (white), sand (light gray), and the grain-size mean as MGS, the MS in SI units (10-6 m3 kg-1), TOC, TOC/TN, δ13C, CaCO3, and selected elements and element ratios from XRF measurements. Additionally, the sample scores on PC1 and PC2 are plotted (See section 4.4). Please note the different scaling of the macro remain and bulk ages as well as of the S values of YU5, and the Fe/S values of YU2. The dashed horizontal lines mark the observed active layer depths.

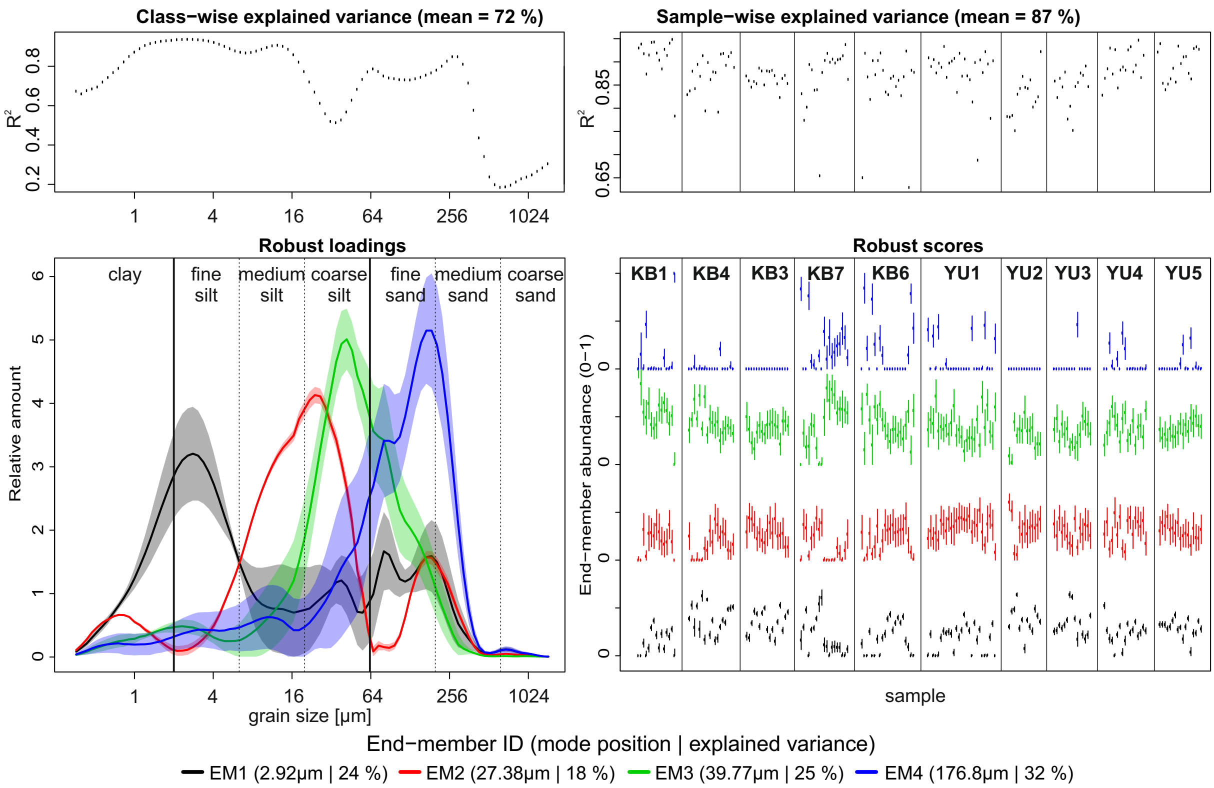

Fig. 8. EMMA results from all input data showing final rEMs and their explained variances, class-wise explained variances, and sample-wise explained variances. The robust scores are plotted with their confidence intervals for each core in their stratigraphic order, i.e. from top (left) to bottom (right).

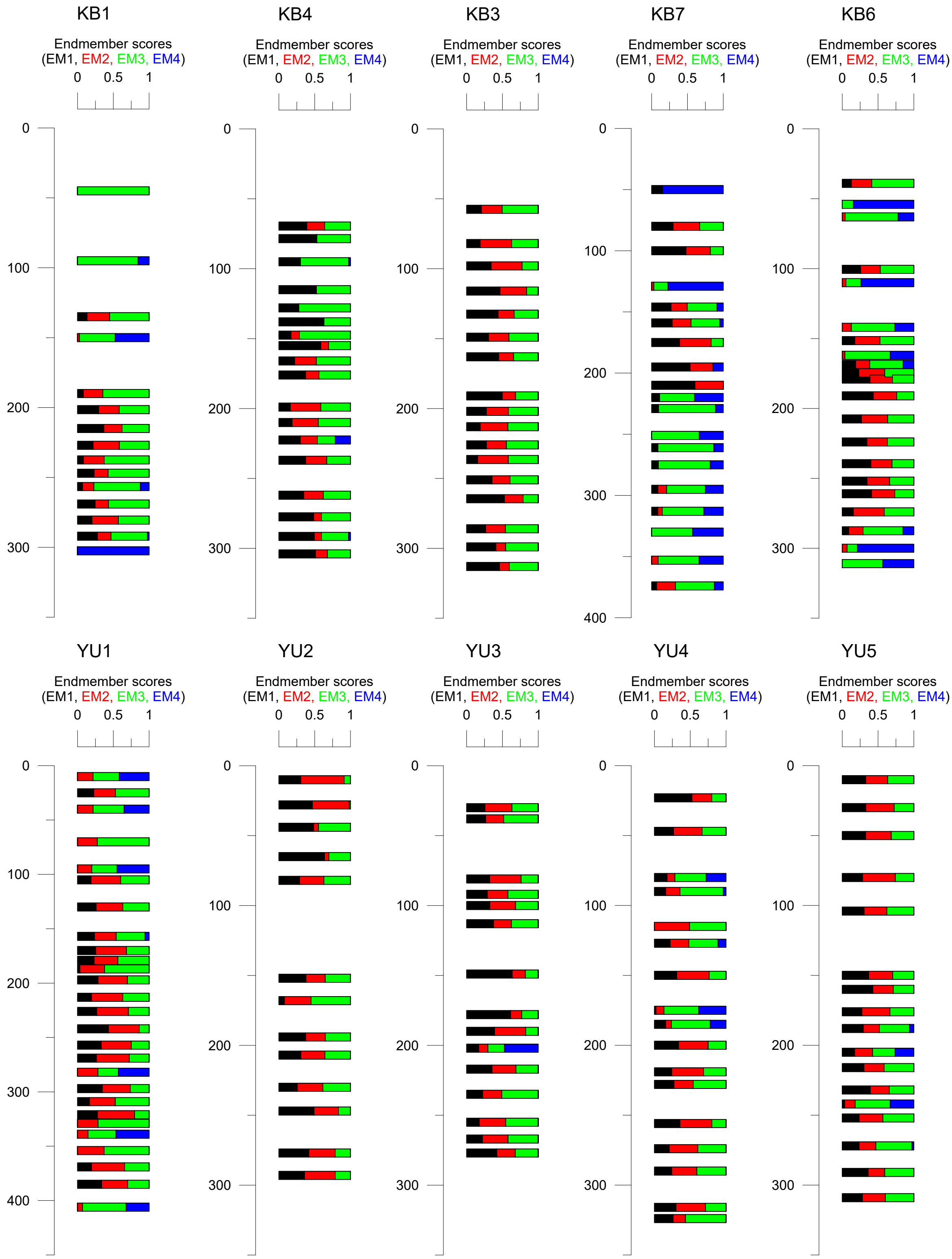

Fig. 9. The mean scores (i.e. the relative contribution of an rEM to each sample) for all studied cores against depth.

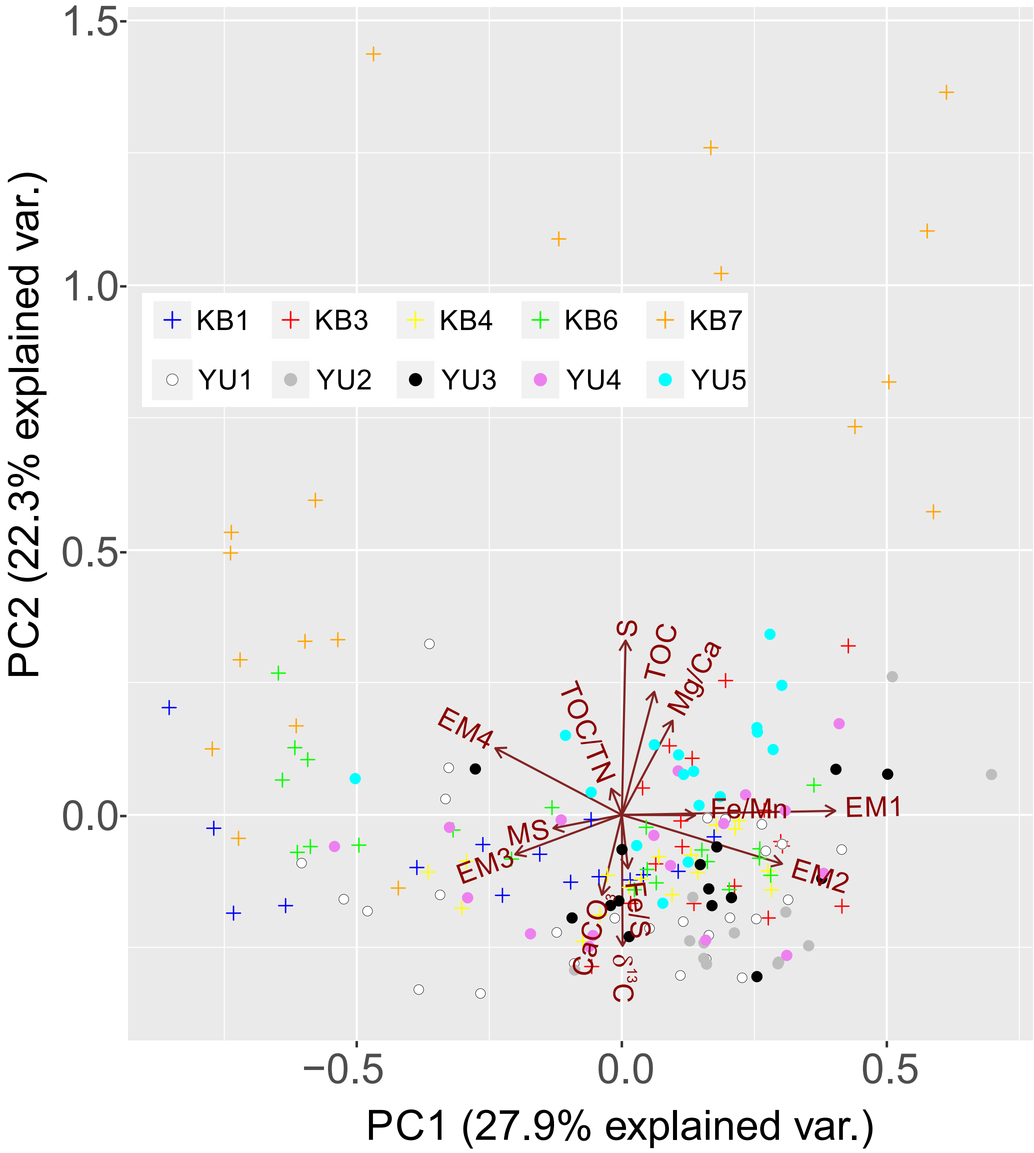

Fig. 10. Ordination plot of the PCA on all rEM scores and biogeochemical parameters for PC1 against PC2. For interpretation purposes, all core samples are additionally projected into the ordination graph.

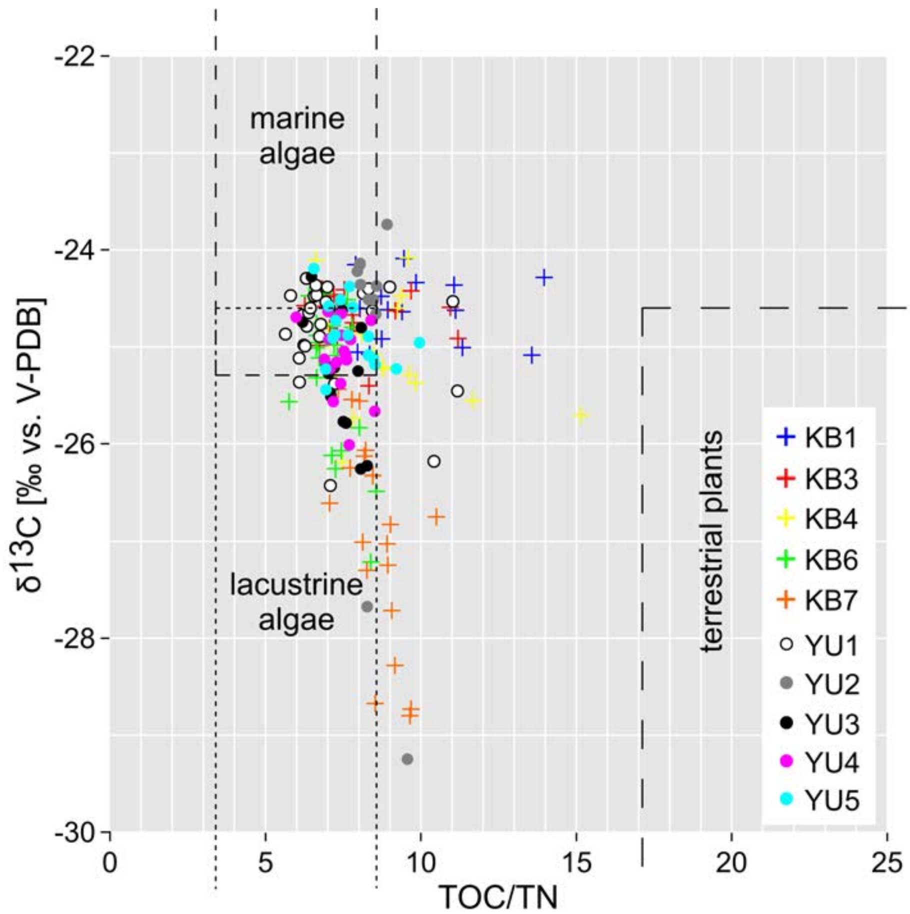

Fig. 11. TOC/TN– δ13C relationship for all core samples reflecting organic matter origin. The classification of organic matter source follows Meyers and Teranes (2001).

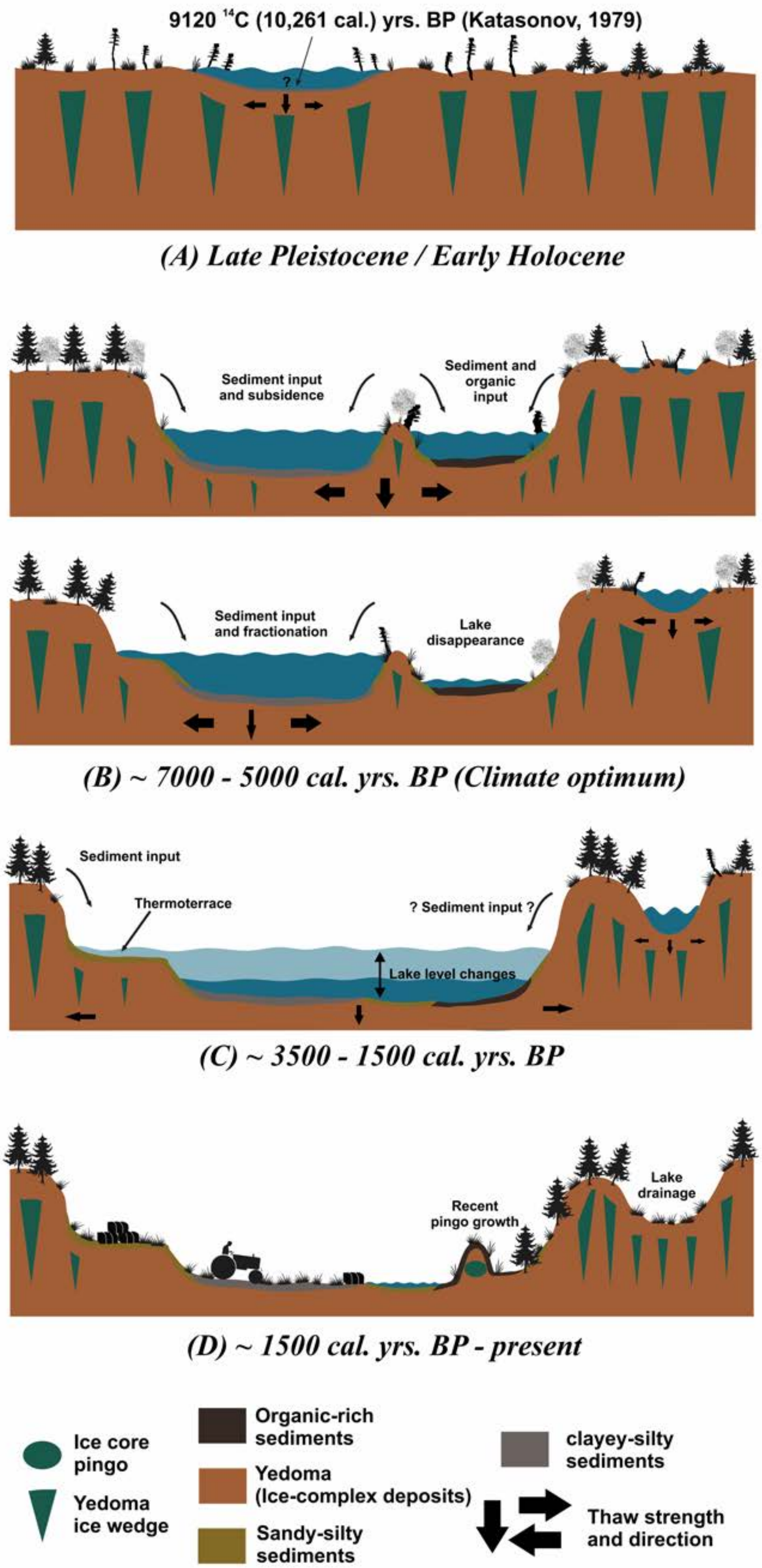

Fig. 12. Schematic diagram showing the generalized thermokarst landscape evolution in CY as inferred from the sedimentology, biogeochemistry, and rEMMA analysis of the two studied thermokarst basins. Drawings are not to scale.

Tables

Tab. 1. Radiocarbon dating results used in this study are ordered due to the dated materials and depth. Dating differences of bulk organic material are additionally highlighted in italics. Calibrated ages refer to the 2σ range.

Lab ID MAMS	**Sample name (including depth in cm bs)**	**Dated material**	**^{14}C ages** yrs BP	(±)	**$\delta^{13}C$ (‰)**	**Calibrated ages** cal. yrs. BP	(±)
		KB Basin edge					
21300	KB1 145-125	Wood	1890	19	-32.9	1812.5	72.5
23115	KB1 222-208	Plant remains	1969	24	-21.0	1930.5	57.5
23116	KB1 243-232	Plant remains	3091	25	-22.6	3314	62
21299	*KB1 55-35*	*Bulk*	*7698*	*27*	*-28.4*	*8482*	*60*
21301	*KB1 145-125 (2)*	*Bulk*	*11,317*	*32*	*-24.7*	*13,207.5*	*91.5*
21302	*KB1 250-244*	*Bulk*	*9619*	*28*	*-24.5*	*1,0978*	*189*
		KB Basin center					
21303	*KB3 63-52*	*Bulk*	*11,024*	*37*	*-24.2*	*12,902.5*	*184.5*
23117	*KB3 205-199*	*Bulk*	*2,8550*	*120*	*-29.1*	*32,877*	*527*
21304	*KB3 222-204*	*Bulk*	*29,660*	*120*	*-31.0*	*34,340*	*400*
21305	*KB3 320-306*	*Bulk*	*33,660*	*160*	*-31.1*	*38,355*	*615*
21306	KB7 60	Plant remains	4984	24	-26.3	5752	102
21307	KB7 154-137	Wood	5587	25	-34.2	6358	51
23120	KB7 243-224	Wood	5735	27	-15.5	6542	91
23121	KB7 285-265	Wood	5767	27	-18.5	6568	75
23122	KB7 320-306	Plant remains	5790	27	-15.5	6582	78
21308	*KB7 264-258*	*Bulk*	*12060*	*40*	*-30.0*	*13910*	*120*
21309	*KB7 382-365*	*Bulk*	*22,210*	*70*	*-30.7*	*26,835*	*645*
		KB Neighboring small drained basin					
23118	KB6 92	Wood	3093	25	-29.5	3316	61
23119	*KB6 295-280*	*Bulk*	*29,190*	*140*	*-26.6*	*33,925*	*575*
		YU Basin edge					
23123	YU1 110-100	Plant remains	4046	25	-27.3	4606	175
21310	*YU1 50-30*	*Bulk*	*9918*	*33*	*-12.5*	*11318.5*	*84.5*
21311	*YU1 219-206*	*Bulk*	*32,670*	*150*	*-28.7*	*37,225*	*585*
23124	*YU1 317-301*	*Bulk*	*16,930*	*60*	*-28.8*	*20,115*	*235*
21312	*YU1 414-398*	*Bulk*	*14,500*	*50*	*-28.8*	*17,595*	*325*
		YU Basin center					
21313	*YU2 91-76*	*Bulk*	*5318*	*25*	*-27.8*	*6092.5*	*91.5*
21314	*YU2 253-240*	*Bulk*	*20,280*	*60*	*-17.1*	*24,185*	*265*
23125	YU3 40-36	Charcoal	3637	26	-27.8	3975	102
23126	YU3 185-170	Plant remains	30,300	140	-17.7	34,865	235
23127	*YU3 226-208*	*Bulk*	*30,500*	*140*	*-15.4*	*34,955*	*275*
		YU Neighboring small drained basin					
23128	YU5 40-20	Plant remains	-189	21	-22.5	modern	
23129	YU5 222-210	Plant remains	34,280	200	-18.6	39,340	650
21315	*YU5 40-20 (2)*	*Bulk*	*23,450*	*90*	*-28.9*	*27,625*	*165*
21316	*YU5 183-170*	*Bulk*	*33,100*	*170*	*-30.3*	*37,290*	*700*
21317	*YU5 318-300*	*Bulk*	*37,080*	*240*	*-28.3*	*41,625*	*405*

Tab. 2. Robust grain-size endmembers, their characteristics, local source as well as transport and accumulation pathways.

Final EM	Mode (µm)	Explained variance (%)	Grain size	Source, transport and accumulation pathways
rEM1	2.9	24	coarse clay to very-fine silt	distal, homogenuous fractionation under lacustrine thermokarst lake conditions
rEM2	27.4	18	medium to coarse silt	distal to proximal, heterogenuous fractionation under lacustrine thermokarst lake conditions and Yedoma background signal
rEM3	39.8	25	coarse silt	proximal, heterogenuous fractionation under terrestrial conditions and Yedoma background signal
rEM4	176.8	32	fine to medium sand	in situ, homogenuous fractionation due to eroding lake shores and basin slopes

Supplementary data for

Holocene thermokarst dynamics in Central Yakutia – A multi-core and robust grain-size endmember modeling approach

Mathias Ulrich*, Heidrun Matthes, Johannes Schmidt, Alexander N. Fedorov, Lutz Schirrmeister, Christine Siegert, Birgit Schneider, Jens Strauss, Christoph Zielhofer

*Corresponding author: Mathias Ulrich, Institute for Geography, Leipzig University, Johannisallee 19a, 04103 Leipzig, Germany. Email: Mathias.Ulrich@uni-leipzig.de

Appendix A.

Additional sedimentological parameters, elements, and elemental ratios for all thermokarst deposit cores that were additionally used for interpretation and discussion of thermokarst (lake) processes.

Appendix B.

PCA ordination plots and explained PC variances on all robust EM scores and biogeochemical parameters for all PCs. For interpretation purposes, all core samples are additionally projected into the ordination graphs.

Appendix A. Table S1. KB1

Depth [cm bs]	Grain size mean [µm]	Grain size sorting	TIC [wt%]	TC [wt%]	TN [wt%]	P [mg/kg]	Ca [mg/kg]	Mn [mg/kg]	Fe [mg/kg]	Zr [mg/kg]
45	26.4	3.9	0.4	1.0	0.0	843.8	27155.0	565.2	28260.0	389,6
95	32.1	4.1	0.4	0.8	0.0	1131.0	29050.0	679.8	27280.0	455,95
135	21.8	4.3	0.0	0.6	0.0	594.5	14825.0	426.7	24835.0	430,95
150	30.7	5.0	0.4	0.9	0.0	1074.5	30480.0	822.0	29280.0	423,15
190	20.9	4.2	0.2	1.2	0.1	836.4	22730.0	619.9	29155.0	426,75
201.5	19.5	4.8	0.3	1.0	0.1	942.0	23445.0	628.4	31570.0	379,5
215	19.0	4.9	0.3	1.0	0.1	926.4	23370.0	601.5	31610.0	372,85
227	18.8	4.4	0.5	1.2	0.1	960.9	30455.0	717.2	30340.0	377,7
237.5	20.1	4.2	0.4	1.1	0.0	857.0	29530.0	619.3	29395.0	395,9
247	18.6	4.3	0.4	1.1	0.0	922.2	28425.0	685.6	30130.0	396,25
256.5	24.8	4.7	0.4	1.0	0.1	892.6	28255.0	683.4	31460.0	366,15
269	19.4	4.5	0.4	1.0	0.1	934.0	26090.0	642.3	31040.0	388,65
280.5	20.2	4.7	0.4	1.2	0.1	988.7	26635.0	650.0	31300.0	369,65
292	21.2	4.9	0.3	1.3	0.1	997.6	24420.0	611.0	30235.0	375,95
302.5	38.5	5.5	0.3	1.0	0.1	961.4	32480.0	633.2	24980.0	345,75
min	18.6	3.9	0.0	0.6	0.0	594.5	14825.0	426.7	24835.0	345,8
max	38.5	5.5	0.5	1.3	0.1	1131.0	32480.0	822.0	31610.0	456,0
mean	**23.5**	**4.5**	**0.4**	**1.0**	**0.1**	**924.2**	**26489.7**	**639.0**	**29391.3**	**393,0**
SD	5.8	0.4	0.1	0.2	0.0	117.3	4197.6	81.3	2136.9	28,4

Appendix A. Table S2. KB4

Depth [cm bs]	Grain size mean [µm]	Grain size sorting	TIC [wt%]	TC [wt%]	TN [wt%]	P [mg/kg]	Ca [mg/kg]	Mn [mg/kg]	Fe [mg/kg]	Zr [mg/kg]
69.5	15.0	4.3	0.2	1.0	0.0	875.0	25175.0	536.1	30215.0	342,25
78.5	16.9	4.5	0.2	0.5	0.0	933.4	19905.0	516.1	29980.0	421,5
95	22.5	4.7	0.7	1.1	0.0	959.6	41715.0	609.3	27970.0	436,15
115	17.0	4.5	0.7	1.1	0.0	891.3	34980.0	706.3	31445.0	329,35
128	20.0	4.5	0.4	0.8	0.0	951.9	28215.0	634.0	29775.0	428,55
138	17.0	4.8	0.5	0.8	0.0	971.1	29000.0	613.0	29500.0	430,6
147.5	21.1	4.5	0.5	0.9	0.0	902.6	31050.0	668.3	30070.0	439,5
155	14.5	4.6	0.5	0.8	0.0	868.7	25900.0	646.7	32075.0	350,4
166	18.7	4.4	0.4	0.8	0.0	884.6	25230.0	651.1	31665.0	358,2
176	16.8	4.4	0.5	0.9	0.0	912.1	28100.0	663.1	32190.0	366,05
199	18.2	4.2	0.8	1.4	0.0	1001.5	41050.0	858.1	31565.0	360,95
210	18.1	4.2	0.8	1.4	0.1	1039.5	42955.0	839.2	31490.0	347,55
222.5	21.1	5.2	0.6	1.1	0.1	940.4	34055.0	697.2	31380.0	354,5
237	17.8	4.8	0.4	0.9	0.1	927.4	25760.0	576.1	31325.0	354,8
262	17.9	4.7	0.6	1.1	0.1	962.3	33155.0	697.3	31695.0	355,85
277.5	16.9	4.9	0.4	0.9	0.1	973.0	25260.0	621.4	31470.0	353,95
291.5	18.9	5.2	0.3	0.9	0.1	902.1	20535.0	537.3	29790.0	330,85
304	16.8	5.1	0.3	0.8	0.1	931.4	21095.0	549.7	30570.0	363,85
min	14.5	4.2	0.2	0.5	0.0	868.7	19905.0	516.1	27970.0	329,4
max	22.5	5.2	0.8	1.4	0.1	1039.5	42955.0	858.1	32190.0	439,5
mean	**18.0**	**4.6**	**0.5**	**1.0**	**0.0**	**934.8**	**29618.6**	**645.5**	**30787.2**	**373,6**
SD	2.0	0.3	0.2	0.2	0.0	44.1	6907.1	91.3	1080.4	37,1

Appendix A. Table S3. KB3

Depth [cm bs]	Grain size mean [µm]	Grain size sorting	TIC [wt%]	TC [wt%]	TN [wt%]	P [mg/kg]	Ca [mg/kg]	Mn [mg/kg]	Fe [mg/kg]	Zr [mg/kg]
57.5	18.1	4.3	0.8	1.2	0.0	845.0	37855.0	673.3	30770.0	379,6
82	17.1	4.1	0.4	0.9	0.0	887.0	26735.0	662.4	33060.0	373,9
98	15.6	4.3	0.4	0.9	0.0	1018.0	28205.0	795.5	35065.0	365,1
116	15.0	4.6	0.4	0.8	0.0	887.3	24610.0	670.9	33365.0	363,1
132.5	16.1	4.5	0.2	0.6	0.0	855.0	17405.0	517.0	31965.0	369,85
149	17.5	4.5	0.2	0.7	0.0	842.6	18165.0	504.9	32915.0	375,45
163	16.3	4.6	0.2	0.8	0.1	860.6	17015.0	533.9	32645.0	379,35
191	15.5	4.5	0.2	1.3	0.1	895.3	18320.0	687.0	31610.0	385,9
202	17.6	4.2	0.6	1.8	0.1	962.8	34670.0	904.2	32320.0	348,4
213	17.8	4.1	0.3	1.5	0.2	974.8	22295.0	752.1	32230.0	380,1
226	17.7	4.3	0.2	1.3	0.1	924.4	15650.0	672.5	32290.0	369,7
236.5	17.8	4.0	0.2	1.3	0.1	943.5	16425.0	681.2	32025.0	379,6
251	16.3	4.3	0.2	1.8	0.2	1056.5	18060.0	1095.0	35315.0	370,9
264.5	14.2	4.3	0.1	1.4	0.2	967.3	12880.0	739.9	34005.0	374,75
286	17.4	4.3	0.0	1.3	0.2	817.4	11685.0	486.5	30190.0	393,5
299	17.1	4.5	0.6	1.6	0.1	1012.0	33480.0	747.2	32030.0	409,35
313	16.3	4.5	0.4	1.6	0.1	1003.5	26230.0	702.1	31440.0	393,75
min	14.2	4.0	0.0	0.6	0.0	817.4	11685.0	486.5	30190.0	348,4
max	18.1	4.6	0.8	1.8	0.2	1056.5	37855.0	1095.0	35315.0	409,4
mean	**16.7**	**4.4**	**0.3**	**1.2**	**0.1**	**926.6**	**22334.4**	**695.6**	**32543.5**	**377,2**
SD	1.1	0.2	0.2	0.4	0.1	70.0	7585.7	145.9	1308.8	13,3

Appendix A. Table S4. KB7

Depth [cm bs]	Grain size mean [µm]	Grain size sorting	TIC [wt%]	TC [wt%]	TN [wt%]	P [mg/kg]	Ca [mg/kg]	Mn [mg/kg]	Fe [mg/kg]	Zr [mg/kg]
50	37.1	6.1	0.0	5.1	0.5	2318.5	8891.5	649.6	42975.0	179,25
80	16.1	4.2	0.0	4.7	0.5	1083.5	10810.0	433.7	27995.0	320,3
100	23.3	5.0	0.0	10.1	0.9	1030.5	10970.0	553.9	26085.0	285,1
129	38.5	5.3	0.0	6.9	0.6	1111.0	12860.0	547.4	27570.0	335
146	21.8	4.7	0.0	7.7	0.7	1302.0	11905.0	579.6	29445.0	286,95
159	20.6	4.9	0.0	6.5	0.6	1641.5	11950.0	618.1	29680.0	301,5
175	15.0	4.4	0.0	6.4	0.5	1449.5	13990.0	585.2	28960.0	303,1
195	18.3	5.8	0.1	6.1	0.6	1893.5	12690.0	669.4	34290.0	225,55
210	11.9	4.7	0.3	4.2	0.4	1924.5	21450.0	1024.0	33350.0	247,4
220	28.9	5.1	0.3	2.4	0.2	1543.0	23265.0	875.7	28695.0	386,35
229	25.0	4.6	0.3	1.4	0.1	1245.5	23535.0	758.4	26135.0	447,05
251	31.2	4.6	0.3	1.5	0.1	1096.0	23260.0	811.2	27355.0	365,5
261	25.2	4.6	0.4	1.2	0.1	1147.5	26610.0	1048.0	29585.0	330,35
275	25.9	4.6	0.4	1.4	0.1	1189.0	28885.0	1029.0	30165.0	386
295	26.4	4.8	0.5	1.5	0.1	1086.5	29495.0	879.0	30985.0	372,8
313	27.1	4.9	0.5	1.4	0.1	1236.5	33480.0	1006.0	29980.0	443,45
330	32.6	4.7	0.6	1.5	0.1	1163.0	36095.0	969.1	29885.0	381,9
353	29.1	4.8	0.8	1.5	0.1	1293.5	47205.0	923.0	27740.0	381,2
374	24.7	4.8	0.9	1.5	0.1	1202.0	47790.0	925.3	28515.0	390,6
min	11.9	4.2	0.0	1.2	0.1	1030.5	8891.5	433.7	26085.0	179,3
max	38.5	6.1	0.9	10.1	0.9	2318.5	47790.0	1048.0	42975.0	447,1
mean	**25.2**	**4.9**	**0.3**	**3.8**	**0.3**	**1366.2**	**22901.9**	**783.4**	**29967.9**	**335,2**
SD	6.8	0.4	0.3	2.7	0.3	340.9	11702.7	192.0	3676.6	69,0

Appendix A. Table S5. KB6

Depth [cm bs]	Grain size mean [µm]	Grain size sorting	TIC [wt%]	TC [wt%]	TN [wt%]	P [mg/kg]	Ca [mg/kg]	Mn [mg/kg]	Fe [mg/kg]	Zr [mg/kg]
39	19.7	4.1	0.5	1.3	0.1	869.3	28645.0	656.9	29540.0	361,65
54	44.0	4.6	0.4	1.0	0.1	1039.0	27295.0	647.5	31680.0	380,1
63	28.4	4.5	0.5	0.9	0.0	996.7	28785.0	661.9	31905.0	364,85
100.5	17.9	4.2	0.5	0.8	0.0	972.9	28910.0	609.2	31725.0	374,95
110	39.3	5.0	0.4	0.8	0.0	933.7	27110.0	589.8	31845.0	376,8
142	28.8	4.5	0.4	1.1	0.1	837.7	24370.0	757.7	33705.0	355,55
151.5	18.3	4.1	0.2	1.1	0.1	873.5	18110.0	671.9	32990.0	368,4
162	29.8	4.6	0.6	1.4	0.1	1009.7	34040.0	704.9	33975.0	366,25
168.5	23.6	4.9	0.5	1.3	0.1	977.1	29415.0	782.9	32385.0	369,65
174.5	18.1	4.2	0.4	1.1	0.1	906.4	26275.0	758.4	32645.0	359,05
179	15.4	4.4	0.3	1.0	0.1	844.9	19965.0	692.2	33055.0	367
191	14.8	4.3	0.2	1.0	0.1	887.9	18020.0	647.5	32605.0	372,05
207.5	16.6	4.3	0.3	1.0	0.1	938.6	20555.0	663.2	31740.0	368,7
224	16.9	4.4	0.4	1.2	0.1	947.0	23740.0	672.6	32085.0	390,85
239.5	15.3	4.4	0.4	1.3	0.1	985.7	24995.0	625.6	32460.0	360,4
252	16.4	4.2	0.5	1.4	0.1	1022.5	28365.0	619.5	32070.0	360,45
261	14.5	4.4	0.5	1.5	0.1	1042.5	27205.0	668.8	32405.0	371,15
274	17.3	4.0	0.4	1.4	0.1	1030.5	23650.0	758.2	33020.0	368,45
287.5	24.9	4.7	0.4	1.3	0.1	1017.1	22625.0	835.9	33575.0	372,3
300	37.0	4.9	0.4	1.0	0.1	951.5	25525.0	709.5	32385.0	359,8
311	32.7	4.6	0.4	0.9	0.1	1005.0	22540.0	646.4	33015.0	355,55
min	14.5	4.0	0.2	0.8	0.0	837.7	18020.0	589.8	29540.0	355,6
max	44.0	5.0	0.6	1.5	0.1	1042.5	34040.0	835.9	33975.0	390,9
mean	**23.3**	**4.4**	**0.4**	**1.1**	**0.1**	**956.6**	**25244.8**	**684.8**	**32419.5**	**367,8**
SD	8.7	0.3	0.1	0.2	0.0	63.7	3948.9	61.2	914.2	8,4

Appendix A. Table S6. YU1

Depth [cm bs]	Grain size mean [µm]	Grain size sorting	TIC [wt%]	TC [wt%]	TN [wt%]	P [mg/kg]	Ca [mg/kg]	Mn [mg/kg]	Fe [mg/kg]	Zr [mg/kg]
10	30.2	5.0	0.2	4.2	0.3	1611.0	24100.0	690.3	31245.0	323,8
25	19.0	4.5	1.7	4.1	0.2	1004.3	62715.0	658.9	28580.0	293,05
40	29.3	4.9	0.9	1.5	0.0	781.8	43865.0	855.5	32725.0	334,95
70	23.0	4.0	0.5	1.0	0.1	863.9	29710.0	741.4	32940.0	373,35
95	30.7	5.0	0.1	0.7	0.1	927.4	17340.0	581.3	36140.0	359,45
105	18.3	4.4	0.3	1.3	0.1	937.5	22815.0	586.8	31470.0	341,4
130	17.9	4.5	0.5	1.0	0.1	962.4	29625.0	715.2	36505.0	346,4
157	21.1	4.9	0.5	1.0	0.1	1067.5	28790.0	736.0	37335.0	343,65
170	17.4	4.5	0.4	0.9	0.1	902.3	24010.0	685.6	36620.0	338,45
179	18.5	4.6	0.4	0.9	0.1	924.7	23950.0	672.2	36040.0	349,6
187	21.1	4.1	0.5	1.0	0.1	891.5	25765.0	609.7	34545.0	349,15
197	17.9	4.7	0.4	0.9	0.1	855.5	22155.0	558.9	33880.0	337,35
213	16.6	3.9	0.1	1.5	0.2	828.3	16060.0	661.1	34060.0	347,15
226	17.4	4.5	0.2	1.5	0.2	949.5	16605.0	796.2	36135.0	342,2
242	15.0	4.4	0.3	1.6	0.2	990.8	21445.0	867.6	36320.0	351,1
257	16.4	4.5	0.3	1.4	0.2	951.7	17465.0	842.7	36370.0	355,75
269	16.1	4.3	0.2	1.4	0.2	953.8	17625.0	767.4	35785.0	369,7
282	31.4	5.0	0.3	1.4	0.1	969.5	20200.0	870.9	35865.0	353,7
297	15.2	4.2	0.5	1.3	0.1	883.4	28880.0	798.4	32705.0	355,5
309	19.4	4.4	0.6	1.1	0.1	909.2	32945.0	743.6	33920.0	352,85
321	14.3	3.9	0.7	1.3	0.1	916.3	37190.0	763.1	33820.0	344,8
329	24.1	3.9	0.6	1.1	0.1	892.9	33065.0	760.9	34200.0	348,85
339	32.7	5.0	0.8	1.3	0.1	847.9	38135.0	655.7	32630.0	338,9
354	22.0	4.1	0.9	1.6	0.1	872.4	46820.0	675.7	31200.0	348,35
369	17.8	4.5	0.8	1.4	0.1	872.7	40315.0	666.2	31790.0	332,35
385	15.1	4.1	0.9	1.6	0.1	947.8	47095.0	651.8	31210.0	340,9
406	32.6	4.4	0.4	1.1	0.1	941.8	26645.0	745.0	33760.0	359,25
min	14.3	3.9	0.1	0.7	0.0	781.8	16060.0	558.9	28580.0	293,1
max	32.7	5.0	1.7	4.2	0.3	1611.0	62715.0	870.9	37335.0	373,4
mean	**21.1**	**4.5**	**0.5**	**1.4**	**0.1**	**942.9**	**29456.7**	**716.9**	**33992.4**	**345,6**
SD	5.9	0.4	0.3	0.8	0.1	143.2	11119.1	85.6	2159.0	14,7

Appendix A. Table S7. YU2

Depth [cm bs]	Grain size mean [µm]	Grain size sorting	TIC [wt%]	TC [wt%]	TN [wt%]	P [mg/kg]	Ca [mg/kg]	Mn [mg/kg]	Fe [mg/kg]	Zr [mg/kg]
10	14.4	4.0	1.3	3.6	0.2	748.3	30250.0	738.4	31525.0	283,45
28	12.7	4.0	0.6	1.4	0.1	671.6	26340.0	613.9	34355.0	273,85
44	15.9	4.2	0.4	0.9	0.1	737.9	25090.0	627.4	31570.0	367,4
65	14.1	4.5	0.2	0.9	0.1	817.5	18890.0	659.1	31555.0	370,6
82	16.7	4.1	0.2	0.7	0.1	936.5	18685.0	707.2	31000.0	377,8
152	15.8	4.3	0.6	1.1	0.0	875.4	30080.0	699.7	32520.0	351,55
168	19.0	4.0	0.5	1.0	0.0	928.4	28085.0	631.7	32930.0	363,75
194	15.7	4.3	0.5	1.0	0.1	885.9	26045.0	601.4	31860.0	363,55
207	15.9	4.2	0.7	1.2	0.1	851.5	31760.0	652.2	32045.0	358,75
230	16.7	4.2	0.6	1.2	0.1	878.0	28100.0	653.0	32365.0	358
247	13.8	4.5	0.9	1.7	0.1	876.9	39645.0	796.7	34000.0	327,2
277	14.8	4.3	0.9	1.7	0.1	924.9	41290.0	730.9	33750.0	328,1
293	14.9	4.2	0.8	1.6	0.1	886.0	36900.0	752.7	33975.0	326,2
min	12.7	4.0	0.2	0.7	0.0	671.6	18685.0	601.4	31000.0	273,9
max	19.0	4.5	1.3	3.6	0.2	936.5	41290.0	796.7	34355.0	377,8
mean	**15.4**	**4.2**	**0.6**	**1.4**	**0.1**	**847.6**	**29320.0**	**681.8**	**32573.1**	**342,3**
SD	1.5	0.2	0.3	0.7	0.0	78.3	6663.0	57.9	1079.1	31,7

Appendix A. Table S8. YU3

Depth [cm bs]	Grain size mean [µm]	Grain size sorting	TIC [wt%]	TC [wt%]	TN [wt%]	P [mg/kg]	Ca [mg/kg]	Mn [mg/kg]	Fe [mg/kg]	Zr [mg/kg]
30	18.4		1.2	1.9	0.1	637.0	38950.0	642.9	31140.0	329,7
38	17.4	4.3	0.5	0.9	0.0	709.9	29600.0	633.5	30535.0	391,05
81	15.6		0.8	1.4	0.1	819.8	36405.0	783.9	34515.0	340,2
92	17.3	4.4	0.8	1.4	0.1	882.0	35215.0	874.9	33890.0	329,95
100	16.1	4.3	0.5	1.2	0.1	1021.0	26270.0	800.5	36135.0	352,2
113	16.7	4.5	0.6	1.2	0.1	1081.0	27845.0	693.1	35505.0	343,75
149	13.7	4.4	0.3	1.3	0.1	914.4	21225.0	646.8	35730.0	344,85
178	14.4	4.5	0.2	1.6	0.2	963.9	19950.0	693.5	34530.0	356,95
190	14.3	4.2	0.5	1.4	0.1	1047.0	27220.0	785.8	34770.0	358,85
202	28.9	5.6	0.5	1.4	0.1	956.6	29920.0	773.2	35065.0	358,05
217	16.0	4.4	0.9	1.9	0.1	999.8	46155.0	760.5	32500.0	349,1
235	18.5	4.3	0.9	1.9	0.1	1021.0	45090.0	729.3	32225.0	337,8
255	18.6	4.2	0.7	1.8	0.1	905.7	37435.0	749.1	33130.0	348,9
267	18.6	4.5	0.9	2.1	0.1	1032.5	44200.0	764.8	31325.0	343,1
277	15.8	4.5	0.7	1.8	0.1	932.8	38025.0	768.9	33860.0	352,6
min	13.7	4.2	0.2	0.9	0.0	637.0	19950.0	633.5	30535.0	329,7
max	28.9	5.6	1.2	2.1	0.2	1081.0	46155.0	874.9	36135.0	391,1
mean	**17.3**	**4.5**	**0.7**	**1.5**	**0.1**	**928.3**	**33567.0**	**740.0**	**33657.0**	**349,1**
SD	3.5	0.3	0.2	0.3	0.0	121.1	8049.6	64.7	1709.9	14,3

Appendix A. Table S9. YU4

Depth [cm bs]	Grain size mean [µm]	Grain size sorting	TIC [wt%]	TC [wt%]	TN [wt%]	P [mg/kg]	Ca [mg/kg]	Mn [mg/kg]	Fe [mg/kg]	Zr [mg/kg]
23	14.4	4.5	1.3	2.0	0.1	677.0	36995.0	690.1	32260.0	319,5
47	17.0	4.3	0.8	1.2	0.0	710.6	32730.0	722.6	32785.0	346,4
80	25.2	5.2	0.6	0.9	0.0	714.5	31385.0	655.6	32370.0	350,8
90	22.2	4.6	0.5	0.8	0.0	848.6	28270.0	604.9	32820.0	356,9
115	20.5	4.0	0.5	0.8	0.0	899.9	26610.0	604.8	33915.0	356,35
127	22.0	5.1	0.5	0.9	0.0	894.5	29430.0	657.1	33985.0	358,2
150	15.6	4.5	0.6	0.9	0.0	890.2	27415.0	646.8	34365.0	343,15
175	29.1	5.0	0.7	1.5	0.1	922.3	35160.0	821.5	33665.0	371
185	25.2	4.9	0.5	1.4	0.1	910.7	26405.0	748.9	34840.0	356,25
200	16.2	4.5	0.2	1.6	0.2	956.9	18890.0	829.0	36210.0	360,45
219	18.9	4.7	0.3	2.0	0.2	1081.5	22180.0	858.5	35925.0	344,35
228	19.3	4.7	0.1	2.1	0.2	1061.0	17730.0	702.9	35315.0	356,1
256	16.6		0.1	2.7	0.3	1057.5	15670.0	729.1	35630.0	337,65
274	18.2	4.3	0.5	2.1	0.2	1131.5	31125.0	723.9	34850.0	338,55
290	19.6	4.7	0.6	2.5	0.2	1215.0	32620.0	761.7	35050.0	354,45
316	15.8	4.4	0.3	2.2	0.2	1055.5	22070.0	785.9	36665.0	349,85
324	20.8	4.7	0.4	1.9	0.2	1124.5	26370.0	772.8	35460.0	350,25
min	14.4	4.0	0.1	0.8	0.0	677.0	15670.0	604.8	32260.0	319,5
max	29.1	5.2	1.3	2.7	0.3	1215.0	36995.0	858.5	36665.0	371,0
mean	**19.8**	**4.6**	**0.5**	**1.6**	**0.1**	**950.1**	**27120.9**	**724.5**	**34477.1**	**350,0**
SD	3.9	0.3	0.3	0.6	0.1	152.4	5956.2	73.6	1321.3	11,1

Appendix A. Table S10. YU5

Depth [cm bs]	Grain size mean [µm]	Grain size sorting	TIC [wt%]	TC [wt%]	TN [wt%]	P [mg/kg]	Ca [mg/kg]	Mn [mg/kg]	Fe [mg/kg]	Zr [mg/kg]
10	17.8	4.7	0.3	1.7	0.1	814.5	29665.0	750.3	34070.0	344,3
30	18.2	4.9	0.2	2.3	0.2	874.9	26335.0	737.7	34095.0	306,2
50	16.0	4.4	0.4	2.2	0.2	897.4	24500.0	678.4	33935.0	328,3
80	16.1	4.3	0.4	2.9	0.3	962.0	24695.0	738.2	34535.0	324,6
104	16.9	4.5	0.4	2.8	0.2	1028.5	29620.0	741.4	33950.0	339,4
150	16.4	4.6	0.1	2.6	0.3	1036.5	16080.0	692.5	33845.0	346,95
160	17.3	4.9	0.3	2.3	0.2	971.8	31205.0	730.3	33470.0	336,4
176	17.0	4.4	0.2	1.9	0.2	935.0	22195.0	752.3	34290.0	345,9
188	21.0	5.1	0.1	1.8	0.2	966.3	17915.0	695.4	33840.0	337,45
205	24.4	5.3	0.2	2.5	0.3	1001.2	19815.0	751.3	34380.0	358,1
216	19.2	4.8	0.1	2.6	0.3	988.3	18655.0	772.8	34020.0	358,05
232	17.7	4.8	0.5	2.2	0.2	963.5	35010.0	811.4	33230.0	369,15
242	27.5	4.9	0.5	2.2	0.2	920.5	30330.0	853.0	33295.0	377,2
252	17.8	4.4	0.5	2.1	0.2	951.1	28755.0	768.6	33560.0	364,45
272	21.2	4.8	0.3	2.0	0.2	938.3	21745.0	797.3	34605.0	357,3
291	19.4	4.9	0.3	2.1	0.2	896.9	22195.0	737.0	33480.0	363,3
309	19.0	4.8	0.5	1.9	0.2	870.4	29625.0	772.9	34000.0	345,05
min	16.0	4.3	0.1	1.7	0.1	814.5	16080.0	678.4	33230.0	306,2
max	27.5	5.3	0.5	2.9	0.3	1036.5	35010.0	853.0	34605.0	377,2
mean	**19.0**	**4.7**	**0.3**	**2.2**	**0.2**	**942.2**	**25196.5**	**751.8**	**33917.6**	**347,2**
SD	3.0	0.3	0.1	0.3	0.0	56.8	5260.4	42.2	396.4	17,3

Appendix B. Figure S1. Ordination plot of PC2 against PC3

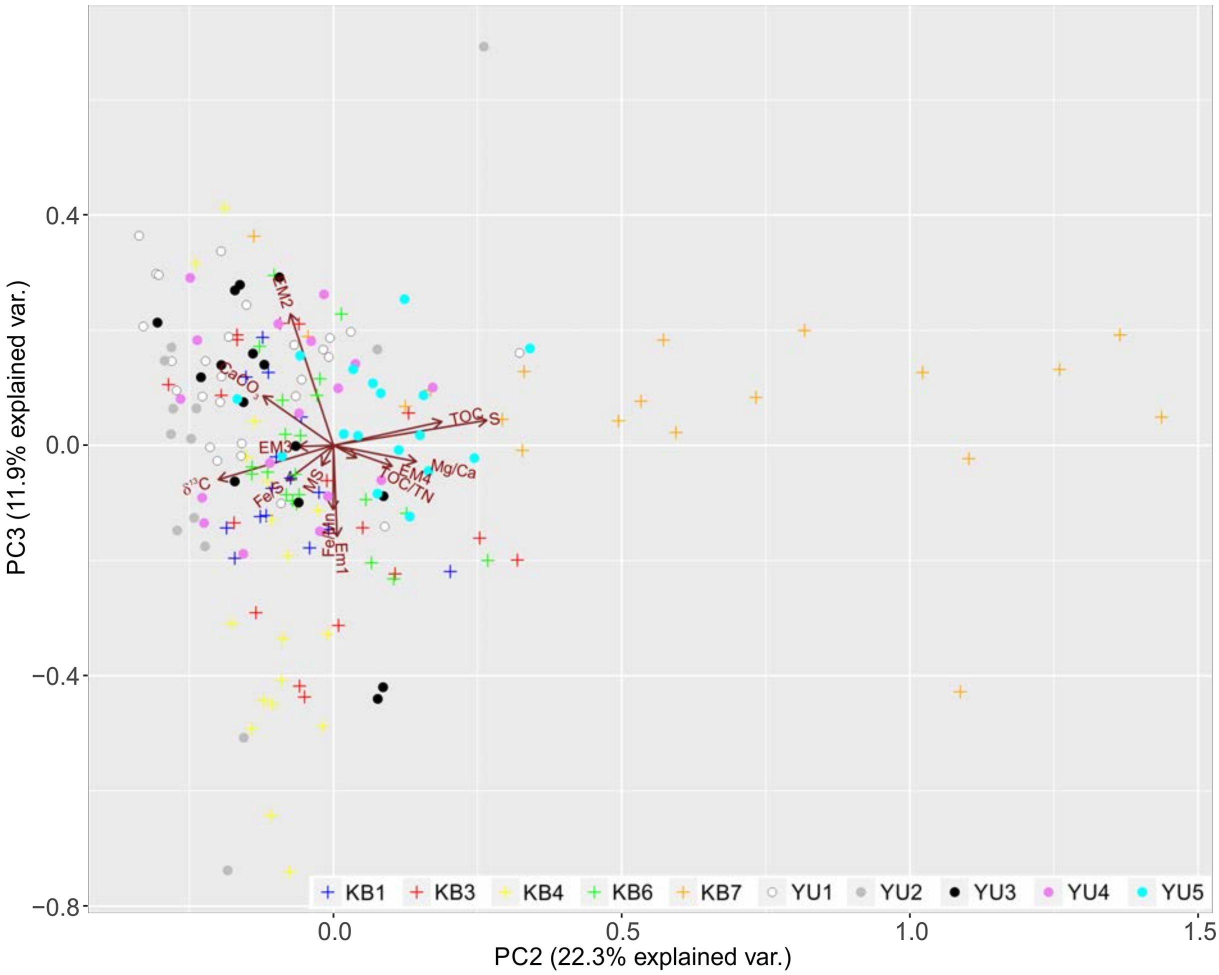

Appendix B. Figure S2. Ordination plot of PC3 against PC4

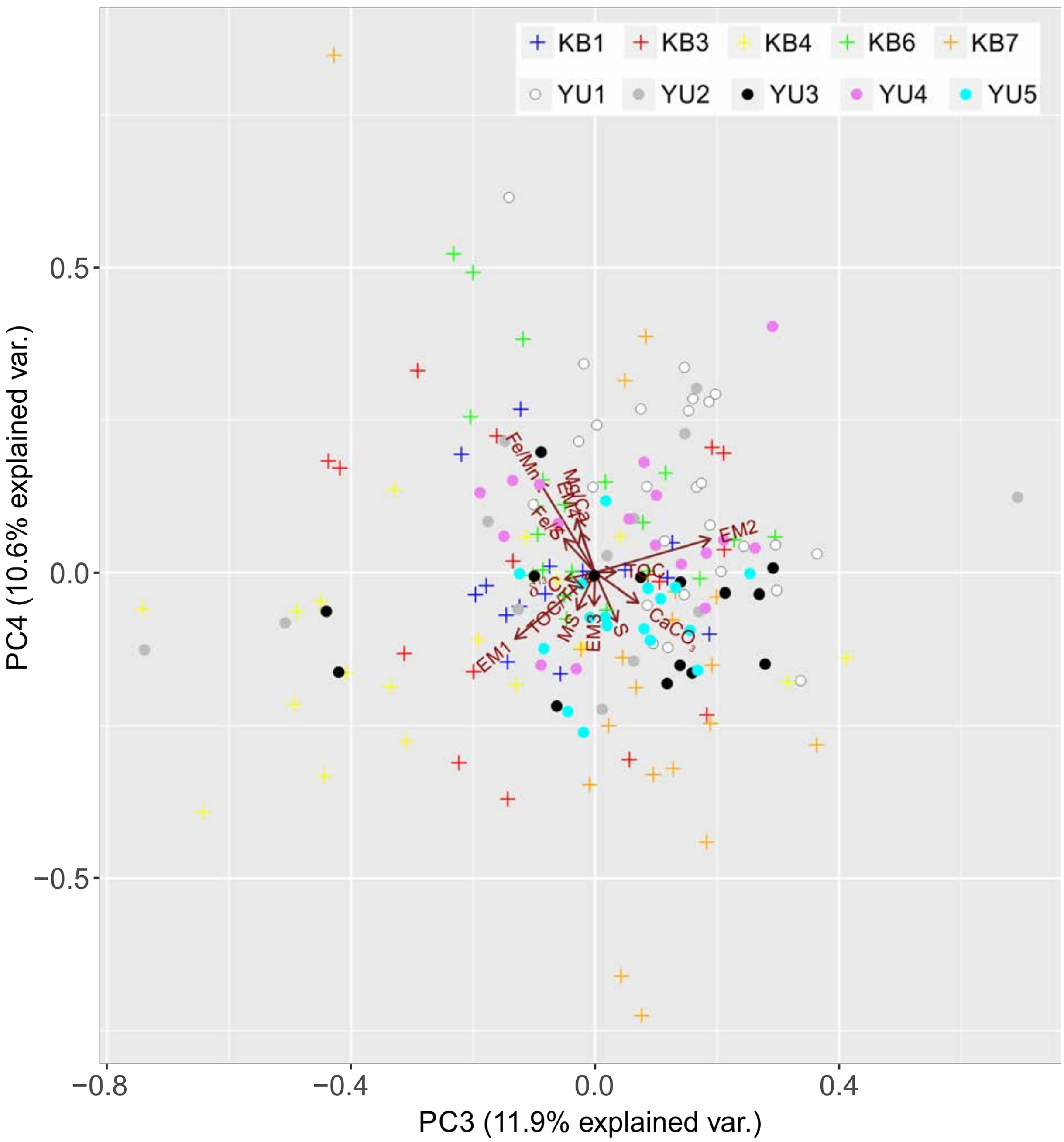

Appendix B. Figure S3. Ordination plot of PC4 against PC5